Testing Turing's theory of morphogenesis in chemical cells

Nathan Tompkins[a], Ning Li[a], Camille Girabawe[a], Michael Heymann[a,b], G. Bard Ermentrout[c], Irving R. Epstein[d], and Seth Fraden[a,1]

Departments of [a]Physics, [b]Biochemistry, and [d]Chemistry, Brandeis University, Waltham, MA 02454; and [c]Department of Mathematics, University of Pittsburgh, Pittsburgh, PA 15260

Alan Turing, in "The Chemical Basis of Morphogenesis" [Turing AM (1952) *Philos Trans R Soc Lond* 237(641):37–72], described how, in circular arrays of identical biological cells, diffusion can interact with chemical reactions to generate up to six periodic spatiotemporal chemical structures. Turing proposed that one of these structures, a stationary pattern with a chemically determined wavelength, is responsible for differentiation. We quantitatively test Turing's ideas in a cellular chemical system consisting of an emulsion of aqueous droplets containing the Belousov–Zhabotinsky oscillatory chemical reactants, dispersed in oil, and demonstrate that reaction-diffusion processes lead to chemical differentiation, which drives physical morphogenesis in chemical cells. We observe five of the six structures predicted by Turing. In 2D hexagonal arrays, a seventh structure emerges, incompatible with Turing's original model, which we explain by modifying the theory to include heterogeneity.

pattern formation | nonlinear dynamics | chemical oscillations | chemical dynamics

The Turing model of morphogenesis offers an explanation for how identical biological cells differentiate and change shape (1). It is difficult to overstate the impact Turing's model has had on developmental biology and the broad field of reaction-diffusion systems (2–9). The Turing model consists of two cases: The first, applicable for a ring of continuous material, has been experimentally confirmed in chemical systems (10–14). The second case, relevant to biology, consists of a ring of discrete cells, each of which contains interacting chemical species that can diffuse to neighboring cells through a chemical selective membrane. However, as the two theories for the cases are different, establishing the Turing model for continuous systems does not prove that the model holds when the chemistry is compartmentalized. Due to challenges in microfabrication, the case of a ring of cells has not previously been experimentally tested in chemical systems. In biology, where networks of cells arise naturally, the Turing model remains controversial because comparison of experiment and theory is hampered by incomplete knowledge of the morphogens involved in development, the rate constants of the reactions, the mechanisms of intercellular coupling, and the role of elasticity (5, 7, 15, 16).

We report an experimental reaction-diffusion system ideally suited for testing Turing's ideas in synthetic "cells" consisting of microfluidically produced surfactant-stabilized emulsions (17, 18) in which aqueous droplets containing the Belousov–Zhabotinsky (BZ) oscillatory chemical reactants (19) are dispersed in oil. In contrast to biology, here the chemistry is understood, rate constants are known, and interdrop coupling is purely diffusive. We explore a large set of parameters through control of concentrations, drop size, spacing, and spatial arrangement of the drops in lines and rings in one dimension and hexagonal arrays in two dimensions. Quantitative comparison of theory and experiment reveals two surprises: A structure not predicted by Turing's analysis is observed, and we measure coupling strengths orders of magnitude weaker than predicted. Nevertheless, in the majority

of cases, we find Turing's model to be exceedingly accurate. Most significantly, we experimentally establish Turing's prediction that interacting identical cells differentiate into chemically distinct populations, which subsequently transform physically in size, thereby demonstrating that these synthetic cells are pluripotent and that abiotic materials can undergo morphogenesis via the Turing mechanism. For one-dimensional arrays of drops, we observe six distinct spatiotemporal patterns, all of which are predicted by the Turing model. In closed-packed 2D arrays, we observe an additional pattern, of a mixed spatial-temporal nature that is incompatible with Turing's original model. We develop a theory, capable of describing this mixed pattern, which posits that the pattern arises from nonlinearity coupled with slight heterogeneity in cellular chemistry and/or coupling strength. As our theory is generic, and heterogeneity is ubiquitous in nature, we expect this pattern to occur in a wide range of reaction-diffusion systems.

The BZ reaction (19), the metal ion-catalyzed oscillatory oxidation of an organic substrate, typically malonic acid (MA), by acidic bromate, has become the prototype of nonlinear dynamics in chemistry (20) and a preferred system for exploring the behavior of coupled nonlinear oscillators (21). Our system (Fig. 1 and Fig. S1) consists of a monodisperse emulsion of drops of aqueous BZ solution, whose diameter ranges from 20 to 200 μm dispersed in a continuous phase of oil (17, 18). The drops are surfactant-stabilized to prevent coalescence (22) (SI Methods). Chemical coupling between drops is mediated through a small subset of less polar intermediates; primarily an inhibitory component, bromine (Br_2), and to a lesser degree, two excitatory components, bromine dioxide ($BrO_2^{\cdot}$) and bromous acid ($HBrO_2$),
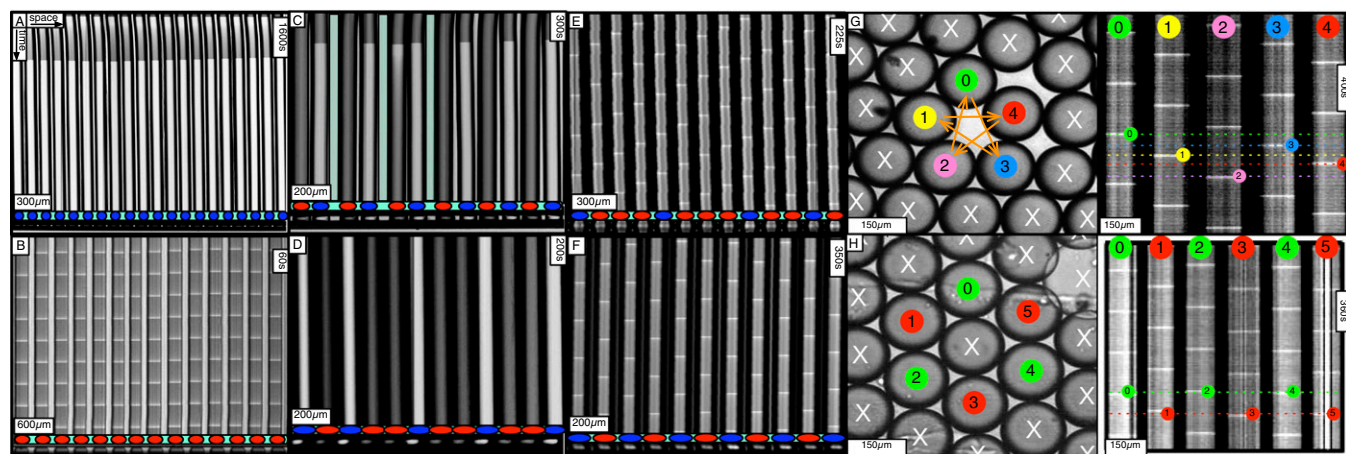
PHYSICS

Fig. 1. Chemical states of linear and circular arrays of BZ drops. See Movies S2 and S3. (*A–F*) Cylindrical capillaries of 100-μm inner diameter filled with a linear array of closely spaced droplets. (*Upper*) Space–time plots demonstrating the corresponding Turing cases (*a–f*) were generated by plotting the intensity of a single line of pixels connecting the centers of adjacent drops as a function of time. (*Lower*) Cartoon above corresponding photograph of droplets. Cartoon colors: blue, BZ drops in oxidized state; red, reduced state; cyan, oil. Chemical conditions: 300 mM bromate, 3 mM ferroin, 0.4 mM Rubpy, and 80 mM sulfuric acid. Malonic acid (MA), NaBr, drop size, and spacing are specified in each case. Five of the six Turing solutions *b–f* are observed. (*A*) Stationary stable oxidized state after initial transient; 10 mM MA, no NaBr, drop size of 130 μm, and oil gap of 20 μm. (*B*) Turing case *b*, (long-wavelength, oscillatory), (q_{min},ω); 2.4 M MA, 10 mM NaBr, drop size of ~230 μm, and oil gap of ~100 μm. (*C*) Turing case *c*, (short-wavelength, stationary), (q_{max},0); 20 mM MA, no NaBr, drop size of ~98 μm, and variable oil gap between 0 and 47 μm. (*D*) Turing case *d*, (intermediate-wavelength, stationary), (*q*,0); 40 mM MA, no NaBr, drop size of 95 μm, and oil gap of ~0 μm (touching drops). (*E*) Turing case *e*, (intermediate-wavelength, oscillatory), (*q*,ω); 640 mM MA, 10 mM NaBr, drop size of 117 μm, and oil gap of 3 μm. (*F*) Turing case *f*, (short-wavelength, oscillatory), (q_{max},ω); 380 mM MA, 10 mM NaBr, drop size of 106 μm, and oil gap of 25 μm. (*G* and *H*) Odd and even circular arrays. Turing case *f*. Rectangular capillaries with cross-section 0.1 mm × 2 mm filled with a 2D array of close-packed droplets from which rings are created with optical isolation. (*Left*) Oscillatory drops are labeled; all other drops are illuminated with light (cross) and held nonoscillatory in the reduced state. (*Right*) Space–time plot. Chemical conditions are as follows: 300 mM bromate, 3 mM ferroin, 80 mM sulfuric acid, 10 mM NaBr, 0.4 mM Rubpy, 640 mM MA; and drop size is ~150 μm. (*G*) Five-membered ring. Drops oscillate in a pentagramal pattern. (*H*) Six-membered ring. Neighboring drops are π radians out-of-phase.

which diffuse from drop to drop through the intervening oil. Here, because the inhibitory bromine strongly partitions into the oil, whereas the excitatory bromous acid does so only weakly, it is possible to satisfy the long-range inhibition and short-range excitation condition needed for the stationary Turing instability (6). Because the system is closed and the BZ reactants are not replenished, the reaction lasts no more than about 100 oscillations until the final uniform equilibrium state is approached. However, the system evolves sufficiently slowly that it can adiabatically exhibit the dynamical instabilities predicted by Turing for open systems (17, 18, 23).

Stationary Turing patterns have been notoriously difficult to produce experimentally, primarily because, for the activator–inhibitor dynamics that typically provides the necessary feedback, the inhibitor must diffuse significantly more rapidly than the activator (6). This condition, which cannot be satisfied with small molecules in homogeneous solution, was first fulfilled, 40 years after Turing's paper, in the chlorite–iodide–malonic acid (CIMA) system, with the activator being complexed to starch, which slows activator transport (11, 12). Stationary Turing states were also observed in a BZ microemulsion consisting of reverse micelles (24, 25). The activator, polar $HBrO_2$, resides in the aqueous interior of the micelle. The inhibitor, nonpolar Br_2, permeates into the oil phase. The transport of the micelles is much slower than the transport of bromine; hence, the criterion for the stationary Turing instability is met. The distinction between the micelles used previously (24, 25) and the emulsions we study here (17, 18) is that the micelles are in dynamic equilibrium; they merge and split on a timescale much shorter than the period of a BZ oscillation and a length scale much shorter than the wavelength of the chemical wave. Therefore, on the timescale and length scale appropriate for a continuum description of the reaction-diffusion system, the BZ microemulsion can be considered to be homogeneous in composition. In this sense, the BZ microemulsion

and the CIMA–starch system share a continuum description. The BZ emulsions studied here are fundamentally different, in that they consist of discrete immobile chemical compartments that never merge. The microfluidic emulsion system presented here is spatially heterogeneous, whereas the micelle and CIMA–starch systems are spatially homogeneous on the relevant timescales.

Model

To quantitatively test the Turing model in discrete cells, it is necessary to control the boundary and initial conditions for all of the cells. We use mixed boundary conditions: Part of the surface enclosing the cells under study consists of other cells in which the chemical concentrations are held constant, and part is a glass wall impenetrable to all chemicals and thereby imposes a no-flux condition. Constant chemical boundaries were created by exploiting the photosensitivity of the BZ catalyst, ruthenium-tris(2,2′-bipyridyl) (Rubpy). Any drop illuminated by blue light is inhibited from oscillating and held in the reduced steady state (*SI Methods*). We produced 1D linear and 2D hexagonal arrays of drops by filling cylindrical and rectangular capillaries, respectively, and used a computer projector coupled to a light microscope to generate patterned illumination (18) in which each drop could be independently illuminated. This flexible illumination system allowed us to isolate either pairs of drops, or a ring of active drops from a 2D array, as shown in Fig. 1 *G* and *H* and Fig. S2, with experimental conditions specified in Table S1. Initial conditions were set by inhibiting all drops with light, as shown in Fig. S3, and then disinhibiting individual selected cells by extinguishing their illumination at prescribed times, thereby allowing the chemical dynamics to proceed. A green light source tuned to the ferroin absorbance wavelength was used to observe, but not affect, the BZ reaction.

To construct a tractable model, Turing assumed cells were chemically uniform, small objects and considered the membranes

Tompkins et al.

separating cells as chemically specific barriers to diffusion, ignoring any chemical reaction or accumulation of chemicals in the membrane. Turing's resulting reaction-diffusion model consists of a ring of point cells diffusively connected directly to nearest neighbors, expressed as a set of equations each of the following form (1):

$$\frac{d\mathbf{c}_i}{dt} = \mathbf{F}_c(\mathbf{c}_i) + \mathbf{M}_c(\mathbf{c}_{i-1} + \mathbf{c}_{i+1} - 2\mathbf{c}_i), \qquad [1]$$

where $\mathbf{c}_i$ is a vector containing the concentrations of the species in the ith cell, $\mathbf{F}_c$ is a vector function describing the kinetics of the c-species, and $\mathbf{M}_c$ is a diagonal matrix containing the coefficients of diffusive transport (μ_c) of the c-species between drops. We describe the chemical kinetics, $\mathbf{F}_c$, of the BZ chemistry with a moel developed by Vanag and Epstein (26, 27) (VE model, *SI Methods*) that considers four concentrations to vary in time: the inhibitory components bromine (Br_2) and bromide (Br^-), the oxidized form of the catalyst (ferriin), and the activator bromous acid ($HBrO_2$). The four VE reaction rates, $\mathbf{F}_c$, contain the aforementioned four variable chemical species, four more chemicals, whose concentrations are approximated as constants in the model, and nine known rate constants; $\mathbf{F}_c$ has zero adjustable parameters. Turing did not specify how the coupling strength μ_c varies with the physical-chemical parameters. To compare theory with experiment, we supplement the Turing model by explicitly calculating the coupling strength between drops in a capillary using Turing's assumptions noted above, with the caveat that different results arise depending on the assumptions used to produce a geometric point model (27, 28):

$$\mu_c = \frac{2D_c P_c(b+d)}{d^2(a+b)} \left(\ln\left(\frac{b+d}{b}\right) + \frac{a-d}{b+d}\ln\left(\frac{a-d}{a}\right) \right). \qquad [2]$$

See Fig. S1 and *SI Methods* for details of the calculation. D_c and P_c are the diffusion and partition coefficients of the c-species in the oil, a is the length of the BZ drop, b is the length of the oil gap separating drops, and d is the diameter of the capillary. The only parameter not measured in Eq. **2** is the partition coefficient of $HBrO_2$, P_x.

To elucidate this model, Turing (1) used linear stability analysis (LSA) and identified six possible chemical structures in rings of diffusively coupled identical cells. In LSA, one characterizes how the steady-state concentrations, i.e., those for which $dc_i/dt = 0$, respond to small perturbations. If all perturbations decay, then the system is in a stable steady state. However, if any perturbations grow with time, the steady state is unstable, and the fastest growing perturbation is labeled a Turing instability. For a ring of N cells, the requirement of periodicity restricts dimensionless wavevectors of the perturbations to take on one of three possible values: $q_{min} = 0$, $q_{max} = 2\pi s_{max}/N$, where for even numbered rings $s_{max} = N/2$ and for odd rings $s_{max} = (N-1)/2$, and $q = 2\pi s/N$, where the integer s ranges from $0 < s < s_{max}$. For each possible q, the perturbation growth can be either oscillatory with frequency $\omega > 0$, or nonoscillatory with $\omega = 0$, giving a total of six possible instabilities. Following Turing's nomenclature, the six instabilities (*a–f*) are each characterized by a wavevector and frequency, (q,ω), as follows: Turing case (*a*), $(q_{min}, 0)$; (*b*), (q_{min}, ω); (*c*), $(q_{max}, 0)$; (*d*), $(q,0)$; (*e*), (q,ω); and (*f*), (q_{max}, ω).

The Turing model, by which we mean the nonlinear rate and coupling equations (Eq. **1**), incorporates two significant and untested approximations: considering each cell as a point and simplification of chemical transport by elimination of explicit consideration of the intracellular medium (the oil in our experiments). Furthermore, the use of LSA introduces an additional, severe approximation. The power of the Turing model is that it provides unambiguous physical mechanisms to explain chemical dynamics and morphogenesis. However, as noted by Turing (1),

"This model will be a simplification and an idealization, and consequently a falsification." This raises the question, to what degree do the Turing model and its LSA describe experiment? The answer to this question is of importance to the broad field of reaction-diffusion systems, as over a thousand papers have been published that have built upon the Turing model, which, before this work, has not been experimentally tested for networks of diffusively coupled cells (4). Here, we address six fundamental questions facing reaction-diffusion systems in general: (*i*) How well does the simplified coupling term, μ_c, agree with experiment? (*ii*) Are there more or fewer than the six predicted Turing linear instabilities? (*iii*) How are the linear instabilities modified by nonlinearities? (*iv*) Does the Turing model provide quantitative and predictive understanding of experiment? (*v*) How do chemical patterns depend on the dimensionality? (*vi*) Do cells sequentially undergo chemical and then physical morphogenesis?

Results

As a first experimental test of the Turing model, Eq. **1**, for cells, we measured the synchronization dynamics of two weakly inhibitory coupled drops at moderate MA concentrations, where uncoupled drops oscillate and bromine can be considered as the sole intercell transporter (18), i.e., $P_x = 0$. We filled cylindrical capillaries with drops, used light both to chemically isolate a pair of adjacent drops and to set the initial phase difference between the isolated drops, and measured the phase difference between the two drops as a function of time, as shown in Fig. S1. Viewed in transmission, the oxidized state appears bright, whereas the reduced state appears dark. Ultimately, the drops synchronize with a phase difference of π radians (18, 29). Fig. S1 and Movie S1 present experimental synchronization rates as a function of drop sizes (50–200 μm) and oil gaps (10–200 μm) for ∼100 drop pairs; for these conditions, rates varied by a factor of 30. Excellent fits were obtained between the experimentally measured synchronization rates and the full nonlinear solution of Eq. **1** if we treated μ_c as a fitting parameter, which varied for each drop size and oil gap. We also fit synchronization rates using the explicitly calculated coupling strength, Eq. **2**. Although the functional form of the coupling strength (Eq. **2**) fit the time-dependent synchronization data well for a wide range of oil gaps and drop diameters, the combination of the Turing model (Eq. **1**) with our explicit calculation of the interdrop coupling (Eq. **2**), overestimates the coupling strength by nearly two orders of magnitude. That is, we replaced μ_c of Eq. **2** with $f\mu_c$, and although theory predicts $f = 1$, experimentally we find $f = 0.0152$. Despite this discrepancy, the fact that only one phenomenological parameter, f, is needed to reconcile theory and experiment over a wide range of coupling strengths is an improvement over the original Turing model, where a different phenomenological parameter, μ_c, is fitted for each drop diameter and oil gap. As a guide to theorists motivated to improve our calculation of the coupling strength, we note that the Turing model assumes a vanishing thin membrane, whereas our experimental system has a finite-sized oil gap. Our model of coupling strength, based on the assumptions of the Turing model, neglects four factors, each of which reduces coupling: nonuniformity in chemical gradients in the drop and the oil, accumulation of chemicals in the oil, time taken to diffuse across the oil, and chemical reactions within the oil.

Having established the Turing model is quantitatively valid for a wide range of synchronization conditions with a single experimentally determined constant in the coupling term, $f = 0.0152$, we prepared a series of one-dimensional arrays of drops in rings and lines and determined the long-term emergent chemical states as a function of the two variables that most strongly control interdrop behavior: MA concentration and coupling strength. Coupling strength, μ_c, is conveniently tuned experimentally by varying the drop size a and oil gap b using microfluidics. In Fig. 1 *A–F*, we illustrate examples of six distinct patterns with

the symmetry corresponding to Turing cases (*a–f*). Five of the six patterns, Fig. 1 *A* and *C–F*, appear where predicted by theory in Fig. 2*B*. Four of the six patterns are identified with Turing cases (*c, d, e, f*). The fifth pattern has the same symmetry as Turing case (*a*). However, this pattern is predicted be a stationary, stable state for MA concentrations below 1 mM and therefore does not arise from a Turing instability, underscoring the point that observation of a chemical state with a pattern corresponding to a Turing instability is insufficient evidence to prove the state arises from a Turing mechanism (3, 6, 8, 30). Notably, the pattern with the symmetry of Turing case (*b*) is observed in a region of parameter space not predicted by theory. This is the sole discrepancy between theory and experiment, and we suspect that it reflects a shortcoming of the VE model. See *SI Discussion* for expanded analysis of each case and Movies S2 and S3 of the spatial-temporal patterns.

The behavior of finite rings depends on the number of drops, *N*, in the ring as seen in Fig. 1 *G* and *H* and Movie S3 for two rings with identical chemical composition, drop size, and spacing, but with five and six drops, respectively. For these particular chemical conditions and for *N* even, LSA predicts antiphase oscillations, corresponding to Turing instability (*f*) characterized by the wavevector–frequency pair (q_{max}, ω), as defined previously and in more detail in *SI Text*. Turing's prediction is that for *N* odd, no two drops will undergo an oxidation transition simultaneously; there will be *N* beats per measure, whereas for *N* even there will be two beats per measure. For a ring of five drops,
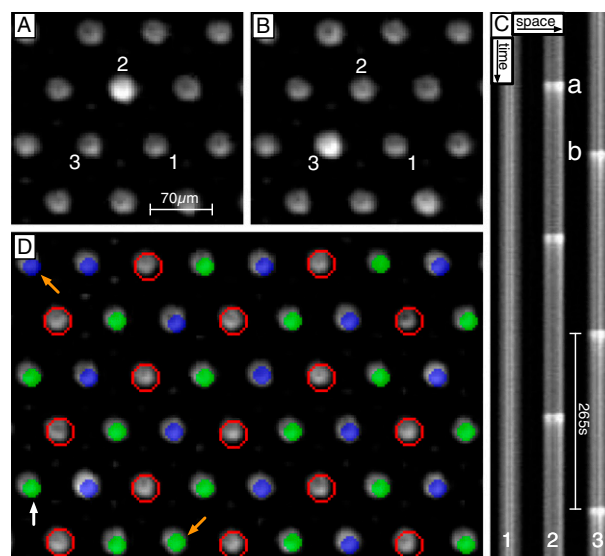

Fig. 3. Observations of 2D arrays of $s0\pi$ states. (*A* and *B*) Single frames demonstrating the $s0\pi$ state. The frames correspond to the first two oxidation transitions, labeled *a* and *b* in *C*. (*C*) Space–time plot of drops 1–2–3 shown in *A* and *B*. Drop 1 is stationary, whereas drops 2–3 remain oscillatory with a phase difference of π. (*D*) A combined image where the stationary drops are outlined in red and the oscillatory drops are color coded by their phase difference, $\phi_i = \theta_i - \theta_{ref}$, where $0 \le \phi \le \pi$ and θ_{ref} is the phase of the drop indicated with the white vertical arrow. Drops where $\phi_i < \pi/2$ are green and $\phi_i > \pi/2$ are blue. Notice that every third drop is stationary, and every oscillatory drop is out of phase with its immediate neighbors; two exceptions are noted with orange arrows. See Movie S6. Chemical conditions: 300 mM bromate, 3 mM ferroin, 0.4 mM Rubpy, 80 mM acid, 640 mM MA, and 10 mM NaBr. Drop size is ~70 µm.

LSA predicts a waveform $C_5(r,t) \propto \exp(i(4\pi r/5 - \omega t))$, with $r \in (0, 1, 2, 3, 4)$ the drop number. In this expression, the phase is chosen such that a drop is oxidized when $4\pi r/5 - \omega t$ is equal to a multiple of 2π. As time advances in increments of one-fifth of a period, the oxidized state in Fig. 1*G* moves along the ring in a pentagramal sequence from drops $0 \to 3 \to 1 \to 4 \to 2$. For the ring of six drops, $C_6(r,t) \propto \exp(i(\pi r - \omega t))$, with $r \in (0, 1, 2, 3, 4, 5)$. As shown in Fig. 1*H*, all even-numbered drops oxidize simultaneously at the beginning of a period, and one-half a period later, all odd-numbered drops oxidize. In Fig. S4 and *SI Methods*, we present the LSA predictions for rings with three, four, five, and six drops and the corresponding experiments. For rings of drops, Turing's LSA theory and our experiments are in complete agreement.

Using published chemical rate constants of the VE model (26) (Eq. S2 and Table S2), we calculate two state diagrams, one using Turing's LSA and the other the full nonlinear simulation (NLS) of equations (Eq. 1) in one dimension, shown in Fig. 2. These theory plots have no adjustable parameters, as the Turing model treats the coupling strength, μ_c, as an independent variable. However, to assign coupling strengths to experiment, we explicitly calculate coupling strength using Eq. 2 to which we introduce a fitting parameter by replacing μ_c of Eq. 2 with $f\mu_c$. We also fit the partition coefficient of the activator, P_x. The best agreement between the NLS and experiment was obtained for $P_x = 0.05$ and $f = 0.14$. With respect to the experimental state diagram, the NLS overestimates coupling strength eightfold, which is the same trend as in the case of the synchronization experiments. In experiments and in the NLS at low MA, we find a stable stationary state in which all of the drops are in-phase. This has the same pattern as Turing state (*a*), but as noted previously, LSA reveals this state is stable and it cannot be considered
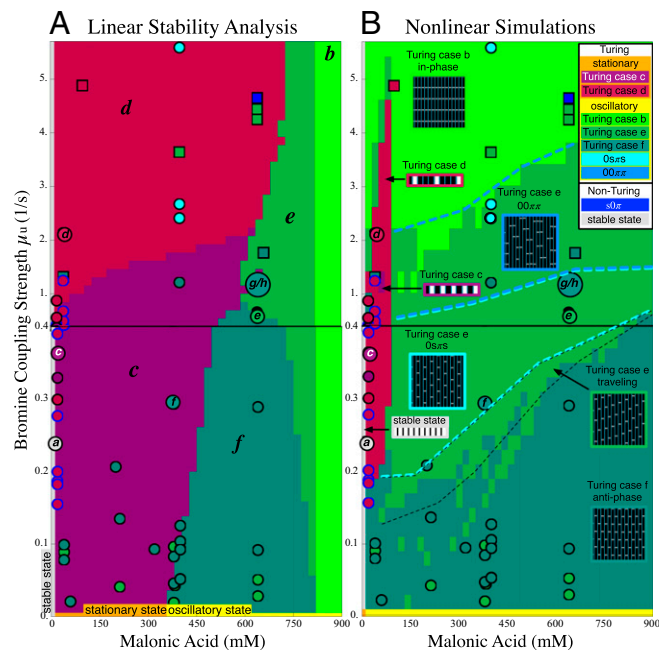

Fig. 2. (*A*) Linear stability analysis (LSA) and (*B*) nonlinear simulations (NLS) of the Vanag–Epstein BZ model, as a function of bromine coupling strength, μ_u, and MA concentration. Note the scale change on the vertical axis at $\mu_u = 0.4$. In both figures, red hues represent stationary states, and green hues, oscillatory states. The data are plotted with circles for 1D experiments and squares for 2D experiments. The red disks outlined in blue indicate a transient initial cluster state settling into a stationary Turing instability. The data points with a letter in the center are included in Fig. 1. Space–time plots of oscillatory states are *Inset* in square areas; stationary states are *Inset* in rectangular areas. The dashed boundaries within the region of Turing case (*e*) of the NLS diagram indicate location of traveling waves, the $0s\pi s$ state (Fig. S6), and the $00\pi\pi$ cluster state. All experimental data points are plotted according to the definitions of μ given in the text with $f = 0.14$. (See *SI Discussion* for more on the plotting of data points.)

Tompkins et al.

Fig. 4. Images and histograms of drops demonstrating morphogenesis plotted as fraction of original drop intensity and fraction of original drop volume. Intensity is a function of the chemical state of the BZ catalyst; bright drops are oxidized, and dark drops reduced. The color-coded line tracks the center of each peak as a function of time. (*A* and *B*) Initially, drops are homogenous in both intensity, or chemical state, and physical volume. (*C* and *D*) At intermediate times, the drops undergo a Turing bifurcation, becoming heterogeneous in oxidation state, but remaining homogenous in volume, as seen by the differentiation into lighter and darker drops of equal size. (*E* and *F*) At later times, drops are heterogeneous in both oxidation state and volume. The oxidized (bright) drops shrink and reduced (dark) drops swell. See Movie S7. Chemical conditions (Table S3): 200 mM MA, 0.4 mM Rubpy, 0 mM NaBr, 80 mM H_2SO_4, 300 mM $NaBrO_3$, 3 mM ferroin, 0.05 × 1-mm rectangular capillary, and initial drop size of ~66 μm.

a Turing state, which arises from a homogeneous unstable state. Both state diagrams predict that as coupling strength increases above zero the same five Turing instabilities (*b–f*) appear with three oscillatory (green hues) and two nonoscillatory (red hues). Theory correctly predicted that for low MA concentration, arrays of large drops would oscillate and that arrays of smaller, chemically identical drops, would be stationary. For 1D arrays of drops in capillaries, the linear and nonlinear theories predict the same basic features, with two notable distinctions. First, nonlinearity strongly suppresses the stationary states. Second, "cluster" states, distinctive oscillating patterns consistent with Turing case (*e*) were experimentally sought and observed only after calculations of the nonlinear state diagram indicated their existence; thus, the Turing model is predictive. Further specific comparisons are included in *SI Discussion*, Figs. S5 and S6, and Movies S4 and S5.

To investigate the effect of dimensionality on Turing instabilities, we performed experiments on close-packed hexagonal arrays of drops, reported as squares in Fig. 2. For conditions intermediate between stationary and oscillatory Turing instabilities, we observed a state, shown in Fig. 3 and Movie S6, that consists of a lattice composed of triangles of drops in which one drop is stationary and the other two oscillate with a phase difference of π, referred to as the $s0\pi$ state (17). LSA requires all drops to share the same temporal behavior, i.e., all stationary, or all oscillatory; thus, the $s0\pi$ state cannot arise from a linear instability. However, it could be a nonlinear effect, but extensive numerical exploration of the full nonlinear chemistry using both the Turing and finite-element models on ordered hexagonal arrays failed to produce the $s0\pi$ state. The qualitative discrepancy between theory and experiment suggests that a critical element is missing from the Turing model. Therefore, we developed a theoretical model for the $s0\pi$ state, valid in general for systems undergoing a Hopf bifurcation, which requires additional conditions

to the Turing model; the drops must be physically or chemically heterogeneous, with two drops that oscillate at a higher frequency than the third and that synchronize out-of-phase when isolated. Our analysis, elaborated in Fig. S7 and in *SI Discussion*, predicts that as the coupling strength between the two higher frequency oscillating drops and the third is increased, there is a transition to a state in which the third drop is stabilized in the nonoscillatory state, whereas the other two drops continue to oscillate out-of-phase. We numerically confirmed our theory by introducing heterogeneity into the Turing and finite-element models, which then produced the $s0\pi$ state. Experimentally, heterogeneity in drop frequency is about 5%, which is less than the 20% required by our simplified analytic theory; therefore, the $s0\pi$ state bears more scrutiny. Only recently has heterogeneity been considered theoretically in reaction-diffusion networks (4, 31–33); our experimental work demonstrates the emergence of a mixed dynamical state caused by a remarkably small amount of heterogeneity. As the mechanism is generic, we expect it to apply to a large class of reaction-diffusion systems. Furthermore, we note that, in general, the experimental state diagram for 2D arrays of drops does not map well onto the one-dimensional nonlinear calculation, indicating that dimensionality plays a significant role in pattern selection.

Turing, in "The Chemical Basis of Morphogenesis" (1), argued that, in case (*d*) (Fig. 1*D*), identical biological cells chemically differentiate into active and inactive stationary states. He further speculated that an activated gene could catalyze an increase in the concentration of intracellular molecules, thereby driving physical differentiation by increasing the osmotic pressure in that cell, causing it to swell. In Fig. 4 and Movie S7, we demonstrate precisely this sequence of chemical differentiation followed by physical morphogenesis in a hexagonal packing of identical drops prepared in the chemical state of Turing case (*d*).

PHYSICS

The drops, produced microfluidically as spheres, are stored in a rectangular capillary and are deformed into cylindrical disks with the same height as the capillary. The intensity of each drop is a monotonic function of the fraction of oxidized BZ catalyst it contains. As shown in Fig. 4*A*, the drops are initially homogeneous in chemistry and drop size. After an initial induction time, the drops undergo a transition from this unstable steady state to Turing case (*d*), in which one out of three drops is in the reduced (dark) state and two out of three are oxidized (bright), shown in Fig. 4*C*. This chemical differentiation occurs with the drop size remaining constant. The oxidized drops consume reagents faster than the reduced drops. This creates an osmotic pressure imbalance, causing water to flow from the oxidized to reduced drops, creating a morphological transformation in which the initially homogeneous cells differentiate into two populations with distinct chemical redox states and physical sizes, as shown in Fig. 4*E*. Quantitative measurements of the volume changes are in agreement with theory, as elaborated in *SI Text*.

Conclusion

Turing's model predicts the circumstances under which initially homogeneous diffusively coupled cells will spontaneously evolve spatiotemporal chemical structures. However, only a small subset of chemical reactions lead to the Turing instabilities; most reactions remain stably homogeneous. In emulsions of the oscillatory BZ chemical reaction, tuning coupling strength and chemical dynamics by changing drop size and MA concentration, respectively, reveals seven distinct chemical structures, six of which were predicted by theory. Turing's model eliminates the oil phase separating cells and treats the coupling strength as a free parameter. We extended Turing's model to explicitly calculate the coupling strength. Experiments revealed that the extended model overestimated intercellular coupling by nearly two orders of magnitude. One experimentally determined parameter was introduced to reconcile theory and experiment for a wide range of conditions; eliminating this one phenomenological parameter remains a theoretical challenge. LSA of the Turing model captures most of the qualitative features of the observed chemical pattern formation, thereby providing a mechanistic explanation of pattern selection. However, the full nonlinear model must be solved to achieve quantitative agreement between experiment and theory. We observe one chemical pattern inconsistent with the original Turing model and propose a generic mechanism whereby slight heterogeneity in the cells leads to a state of mixed dynamical and stationary character. The Turing model is regarded as a metaphor for morphogenesis in biology, useful for a conceptual framework and to guide modeling, but not for prediction (7). In contrast, in this chemical system, we demonstrated that the Turing model quantitatively explains "materials morphogenesis" in which cellular compartments first chemically and then physically differentiate, raising the possibility of exploiting this form of reaction-diffusion chemistry for materials science applications.

1. Turing AM (1952) The chemical basis of morphogenesis. *Philos Trans R Soc Lond* 237(641):37–72.
2. Karsenti E (2008) Self-organization in cell biology: A brief history. *Nat Rev Mol Cell Biol* 9(3):255–262.
3. Kondo S, Miura T (2010) Reaction-diffusion model as a framework for understanding biological pattern formation. *Science* 329(5999):1616–1620.
4. Mendez V, Fedotov S, Horsthemke W (2010) *Reaction-Transport Systems: Mesoscopic Foundations, Fronts, and Spatial Instabilities* (Springer, Berlin).
5. Müller P, et al. (2012) Differential diffusivity of Nodal and Lefty underlies a reaction-diffusion patterning system. *Science* 336(6082):721–724.
6. Meinhardt H (2012) Turing's theory of morphogenesis of 1952 and the subsequent discovery of the crucial role of local self-enhancement and long-range inhibition. *Interface Focus* 2(4):407–416.
7. Reinitz J (2012) Pattern formation: Turing at 100. *Nature* 482(7386):464.
8. Morelli LG, Uriu K, Ares S, Oates AC (2012) Computational approaches to developmental patterning. *Science* 336(6078):187–191.
9. Schweizer J, et al. (2012) Geometry sensing by self-organized protein patterns. *Proc Natl Acad Sci USA* 109(38):15283–15288.
10. Noszticzius Z, Horsthemke W, McCormick WD, Swinney HL, Tam WY (1987) Sustained chemical waves in an annular gel reactor. *Nature* 329(6140):619–620.
11. Castets V, Dulos E, Boissonade J, De Kepper P (1990) Experimental evidence of a sustained standing Turing-type nonequilibrium chemical pattern. *Phys Rev Lett* 64(24):2953–2956.
12. Ouyang Q, Swinney HL (1991) Transition from a uniform state to hexagonal and striped Turing patterns. *Nature* 352(6336):610–612.
13. Epstein IR, Pojman JA (1998) *Introduction to Nonlinear Chemical Dynamics. Oscillations, Waves, Patterns and Chaos* (Oxford Univ Press, New York).
14. Horváth J, Szalai I, De Kepper P (2009) An experimental design method leading to chemical Turing patterns. *Science* 324(5928):772–775.
15. Inaba M, Yamanaka H, Kondo S (2012) Pigment pattern formation by contact-dependent depolarization. *Science* 335(6069):677.
16. Li A, et al. (2013) Shaping organs by a wingless-int/Notch/nonmuscle myosin module which orients feather bud elongation. *Proc Natl Acad Sci USA* 110(16):E1452–E1461.
17. Toiya M, González-Ochoa HO, Vanag VK, Fraden S, Epstein IR (2010) Synchronization of chemical micro-oscillators. *J Phys Chem Lett* 1(8):1241–1246.
18. Delgado J, et al. (2011) Coupled oscillations in a 1D emulsion of Belousov-Zhabotinsky droplets. *Soft Matter* 7(7):3155–3167.
19. Zaikin AN, Zhabotinsky AM (1970) Concentration wave propagation in two-dimensional liquid-phase self-oscillating system. *Nature* 225(5232):535–537.
20. Field RJ, Burger M (1985) *Oscillations and Traveling Waves in Chemical Systems* (Wiley, New York).
21. Fukuda H, Morimura H, Kai S (2005) Global synchronization in two-dimensional lattices of discrete Belousov-Zhabotinsky oscillators. *Physica D* 205(1):80–86.
22. Holtze C, et al. (2008) Biocompatible surfactants for water-in-fluorocarbon emulsions. *Lab Chip* 8(10):1632–1639.
23. Toiya M, Vanag VK, Epstein IR (2008) Diffusively coupled chemical oscillators in a microfluidic assembly. *Angew Chem Int Ed Engl* 47(40):7753–7755.
24. Vanag VK, Epstein IR (2001) Pattern formation in a tunable medium: The Belousov-Zhabotinsky reaction in an aerosol OT microemulsion. *Phys Rev Lett* 87(22):228301.
25. Epstein IR, Vanag VK (2005) Complex patterns in reactive microemulsions: Self-organized nanostructures? *Chaos* 15(4):047510.
26. Vanag VK, Epstein IR (2009) A model for jumping and bubble waves in the Belousov-Zhabotinsky-aerosol OT system. *J Chem Phys* 131(10):1–7.
27. Vanag VK, Epstein IR (2011) Excitatory and inhibitory coupling in a one-dimensional array of Belousov-Zhabotinsky micro-oscillators: Theory. *Phys Rev E Stat Nonlin Soft Matter Phys* 84(6):066209.
28. Vanag VK, Epstein IR (2003) Diffusive instabilities in heterogeneous systems. *J Chem Phys* 119(14):7297–7307.
29. Kuramoto Y (1984) *Chemical Oscillations, Waves and Turbulence* (Springer, Berlin).
30. Maini PK, Baker RE, Chuong CM (2006) Developmental biology. The Turing model comes of molecular age. *Science* 314(5804):1397–1398.
31. Colizza V, Pastor-Satorras R, Vespignani V (2007) Reaction-diffusion processes and metapopulation models in heterogeneous networks. *Nat Phys* 3(4):276–282.
32. Nakao H, Mikhailov A (2010) Turing patterns in network-organized activator-inhibitor systems. *Nat Phys* 6(7):544–550.
33. Wolfrum M (2012) The Turing bifurcation in network systems: Collective patterns and single differentiated nodes. *Physica D* 241(16):1353–1357.

Supporting Information

Tompkins et al. 10.1073/pnas.1322005111

SI Text

This document is intended as a source of supplementary information. Each section is intended to provide necessary details for other researchers wishing to critically analyze our techniques or replicate our findings. The document as a whole is not intended to have a continuous narrative or further a specific argument.

SI Methods

Additional theoretical and experimental methods with background information used in the preparation of the main text are included in this section.

Coupling Strength. A key assumption in the Turing model is that cells are diffusively coupled, as characterized by the diffusive rate, μ_c, where $dc_i/dt = \mu_c(c_{i-1} + c_{i+1} - 2c_i)$, with c_i the concentration of a single chemical species in the ith cell. However, Turing did not specify a form for the coupling term μ, so it is treated as a fitting parameter in comparison of theory with experiment. We supplement Turing's model by calculating how the coupling term depends on our system's physical and chemical parameters.

Following Turing, our model consists of a ring of identical cells, which are considered to be small enough so that diffusion makes the concentration inside each cell uniform on a timescale that is much shorter than any chemical reaction dynamics. To calculate μ_c, we first consider a one-dimensional case, illustrated in Fig. S1C. Consider two cells each with an aqueous dimension of length a separated by an oil gap of length b such that the total center to center distance is $a + b$. Again, like Turing, we assume that no chemical species accumulate in the oil phase. Conservation of mass demands that $\partial c/\partial t = -\partial J/\partial x$, where c is the concentration and J is the concentration flux. Additionally, Fick's first law states that $J = -D\nabla c$. When discretized we have the following:

$$\frac{\Delta c}{\Delta t} = -\frac{\Delta J}{\Delta x} = \frac{J_{i-1,i} - J_{i,i+1}}{a},$$

where we make the additional assumption that the concentration is uniform within the aqueous phase, so the only fluxes are across the oil gaps:

$$J_{i-1,i} = \frac{DP_c}{b}(c_{i-1} - c_i) \quad J_{i,+1i} = \frac{DP_c}{b}(c_i - c_{i+1}),$$

which, when substituted into our conservation of mass equation yields the following:

$$\frac{\Delta c}{\Delta t} = \frac{DP_c}{ab}(c_{i-1} + c_{i+1} - 2c_i) \Rightarrow \mu_c = \frac{DP_c}{ab},$$

where D is the diffusion constant in oil for chemical species c, and P_c is the oil/water partition coefficient for species c. For our analysis, we used the values $D = 3 \times 10^{-9} m^2/s$, $P_x = 0.05$, $P_y = P_z = 0$, and $P_u = 2.5$.

The above result for μ_c was derived for cells on a line in one dimension. Experimentally, our Belousov–Zhabotinsky (BZ) drops confined in cylindrical capillaries resemble spherocylinders. We can improve on the previous result by using the Derjaguin approximation to calculate the diffusive flux between two spherocylinders confined in a cylindrical capillary of diameter d. From the geometry of Fig. S1D, we know that the gap β at any point is

$\beta = b + 2\Delta$, where $\rho^2 + (r - \Delta)^2 = r^2$. We can solve for Δ and find $\Delta = r \pm \sqrt{r^2 - \rho^2}$. As $\Delta \to 0$ when $r \to \infty$ we can state the following:

$$\Delta = r - \sqrt{r^2 - \rho^2}.$$

Thus, we know β as a function of ρ is as follows:

$$\beta = b + 2\left(r - \sqrt{r^2 - \rho^2}\right).$$

As $a + b$ is a constant, and from the geometry we can see that $\alpha + \beta$ is the same constant, we can write α as a function of ρ as follows:

$$\alpha = a - 2\left(r - \sqrt{r^2 - \rho^2}\right).$$

To apply the Derjaguin approximation, we calculate the average flux in cylindrical coordinates from the following:

$$\mu_c = \frac{1}{A}\int_\theta \int_\rho \mu_c(\rho)\rho d\rho d\theta,$$

which when the proper symmetries are applied becomes the following:

$$\mu_c = \frac{2}{r^2}\int_0^r \mu_c(\rho)\rho d\rho.$$

Using the form of μ_c derived above and replacing the drop width a with $\alpha(\rho)$ and the gap size b with the gap $\beta(\rho)$, we have the following:

$$\mu_c = \frac{2}{r^2}\int_0^r \frac{DP_c}{\alpha(\rho)\beta(\rho)}\rho d\rho,$$

which in experimental units of d is the following:

$$\mu_c = \frac{8}{d^2}\int_0^{\frac{d}{2}} \frac{DP_c}{\left(a - d + 2\sqrt{\frac{d^2}{4} - \rho^2}\right)\left(b + d - 2\sqrt{\frac{d^2}{4} - \rho^2}\right)}\rho d\rho.$$

Solving the integral yields the following:

$$\mu_c = \frac{2DP_c(b+d)}{d^2(a+b)}\left(\ln\left(\frac{b+d}{b}\right) + \frac{a-d}{b+d}\ln\left(\frac{a-d}{a}\right)\right).$$

This model is valid for unconfined drops with a diameter greater than, or equal to, the capillary diameter. When the drops are spheres with a diameter equal to the capillary diameter, $(a = d)$:

$$\mu_c = \frac{2DP_c}{a^2}\ln\left(\frac{a+b}{b}\right).$$

In the weak coupling limit of spherical drops separated by a great distance, $a \ll b$, the result simplifies further to the following:

$$\mu_c = \frac{2DP_c}{ab}.$$

This last result is similar to the coupling strength in 1D; the factor of 2 difference comes from the circular shape of the drop in the capillary.

We cannot directly measure μ_c and so instead examine the effect that coupling has on the dynamics of two weakly coupled chemical oscillators. An individual BZ drop oscillates on a limit cycle. If two oscillators are weakly coupled, then, to first order, they remain on the limit cycle, but synchronize with a phase difference of either 0 or π radians. In the limit of weak coupling, the dynamics of the phase difference between two coupled drops evolves exponentially with rate constant, z, proportional to the coupling strength. To perform the corresponding experiments, we fill cylindrical capillaries with drops and use light to chemically isolate a pair of adjacent drops (Fig. S1A). The phase difference between the two drops is measured as a function of time, from which the rate of synchronization z is measured (Fig. S1E). For each measured rate constant z, we calculate a theoretical rate constant z_{th} by integrating Eqs. **1** and **2**. Measured and calculated rate constants for a wide range of drop sizes and separations are compared in Fig. S1 F and G. To compare experimentally measured synchronization rates to rates calculated from the full nonlinear solution of Eqs. **1** and **2**, given in the main text, we introduced one adjustable parameter, f, in Eq. **2**, by replacing μ_c with $f\mu_c$. Although the functional form of the coupling strength (Eq. **2**) fits the time-dependent synchronization data well for a wide range of oil gaps and drop diameters, the combination of the Turing model (Eq. **1**) with our explicit calculation of the interdrop coupling (Eq. **2**), overestimates the coupling strength by nearly two orders of magnitude; although theory predicts $f = 1$, experimentally we find $f = 0.0152$.

On the one hand, our theory of coupling strength is not very good, giving a deviation between theory and experiment of a factor of 60. On the other hand, it is an improvement over Turing's model in which no functional form of μ_c is given, requiring that μ_c must be experimentally determined for each combination of drop size and spacing. Our model requires making only one measurement for an arbitrary drop size and spacing to determine the coupling strength by measuring f. Once that single fitting parameter is obtained, then $f\mu_c$, with μ_c given by Eq. **2**, can be used to predict all other coupling strengths as a function of drop size and spacing.

Experimental Apparatus. The emulsion is illuminated by two sources, a 510-nm filtered Köhler illumination setup for imaging and a modified commercial data projector for photoinhibition. Imaging is done at 510 nm, as this wavelength does not interact with the ruthenium-tris(2,2′-bipyridyl) (Rubpy), is opaque to ferroin, and is transparent to ferriin. Thus, 510 nm is passive imaging where the oxidation state of each drop is immediately viewable by its transmission intensity. The commercial projector is only modified to focus through the microscope objective; the light source and color functionality are unaltered, as Rubpy is sensitive to 450-nm light, which is within the projector's RGB "blue" output. Optical isolation is achieved by Matlab code written by the group, which tracks each drop for movement and places a dot of blue light over the center of every drop that is to be inhibited. The size, intensity, and duty cycle of the illumination are determined by empirically establishing the minimum inhibitory exposure for each experimental condition.

Drop Making. We generate our drops using flow focusing microfluidic poly(dimethylsiloxane) chips designed and manufactured by the group using standard methods. The BZ reactants are introduced in two separate streams to prevent the reaction from starting before on-chip mixing. One stream contains the catalysts and bromate, whereas the other stream contains the acids and bromide. The exact dimensions and flow rates vary based on the desired drop size. The oil used is a commercially available fluorocarbon oil (3M; HFE 7500) stabilized by a surfactant designed by the Weitz Group at Harvard (obtained from RainDance Technologies, the Weitz Laboratory, and RAN Biotechnologies). The drops typically have a coefficient of size variation of about 1%. When loaded into a rectangular capillary of height slightly less than the drop diameter, the drops self-assemble into a closed-packed 2D hexagonal lattice. See Table S1 for the chemical and physical parameters used for the experimental data presented in the main text.

Optical Isolation. We add the photosensitive catalyst Rubpy to the BZ mix, which has the effect that, as long as blue light is shone on the drops, they are held in the reduced steady state. Therefore, light can be used to create constant chemical boundary conditions for networks of nonilluminated drops. We use a computer projector coupled to a light microscope to generate patterned illumination and isolate a ring of active drops from a 2D array as shown in Fig. S2. In experiments, a duty cycle of 3 s on/7 s off is used for optical inhibition. As the BZ oscillation frequency is at least an order of magnitude less than the inhibition frequency, the temporal variation in the light is effectively averaged. Data are collected while the inhibitory light is off.

This method can also be used to probe the range of interaction between drops. If all but drops 1 and 2 in Fig. S2 are illuminated, these two adjacent drops synchronize, but if all but drops 1 and 3, or all but drops 1 and 4 are illuminated, then the phase difference between these drops increases linearly in time, demonstrating that nearest neighbor drops are coupled, whereas next nearest neighbors are uncoupled. Single drops, optically isolated from all others, differ in frequency by less than 3%, as illustrated by the fact that about 40 cycles are required for a phase difference of 2π to develop between nonadjacent drops.

Initial Conditions. Another feature of adding the photosensitive catalyst Rubpy to the BZ mix beyond the ability to set boundary conditions is the ability to set the initial conditions. By exposing the entire system to a bright pulse of light, we can "reset" the phase of all of the oscillators to create an initial in-phase state as seen experimentally in Fig. S3. Depending on the chemical conditions of the system, this state may or may not be stable.

Data Analysis. Data are analyzed in real time during data acquisition using Matlab code written by the group, which algorithmically detects each drop and calculates the average pixel value for each drop in each frame. For each drop, a time series of pixel values is used to determine the periodic peaks, which correspond to the oxidation spikes of the BZ reaction. These spikes are defined as phase zero, and the interspike interval is used to define the period for that oscillation and to linearly define the phases between each spike. The period and phase information can then be used by the data acquisition code in determining which drops are to be inhibited and when. Further postacquisition data analysis is possible by calculating an order parameter for each upright triangle of drops using the phases or phase differences.

Linear Stability Analysis. The linear stability analysis (LSA) for a periodic ring of N cells is performed using the four-variable Vanag–Epstein (VE) model. We begin with the reaction-diffusion equation (Eq. **1**) from the main text:

$$\frac{d\boldsymbol{c}_r}{dt} = \boldsymbol{F}_c(\boldsymbol{c}_r) + \boldsymbol{M}_c(\boldsymbol{c}_{r-1} + \boldsymbol{c}_{r+1} - 2\boldsymbol{c}_r), \qquad \textbf{[S1]}$$

where $\boldsymbol{c}_r$ is a vector containing the concentrations of the chemical species in the rth cell, $\boldsymbol{F}_c$ is a vector function describing the

chemical kinetics of the c-species, and M_c is a diagonal matrix containing the coefficients of diffusive transport (μ_c) of the c-species from drop to drop (2). For the VE model with four concentrations, $c = (x, y, z, u)$, and F_c is given as follows:

$$f_1(x,y,z) = -k_1xy + k_2y - 2k_3x^2 + k_4x(c_0-z)/(c_0-z+c_{min})$$
$$f_2(x,y,u) = -3k_1xy - 2k_2y - k_3x^2 + k_7u + k_9z$$
$$f_3(x,z) = 2k_4x(c_0-z)/(c_0-z+c_{min}) - k_9z - k_{10}$$
$$f_4(x,y,z) = 2k_1xy + k_2y + k_3x^2 - k_7u,$$

$$\text{[S2]}$$

with the constants and variables defined in Table S2. The coupling matrix is as follows:

$$M_c = \begin{pmatrix} \mu_x & 0 & 0 & 0 \\ 0 & \mu_y & 0 & 0 \\ 0 & 0 & \mu_z & 0 \\ 0 & 0 & 0 & \mu_u \end{pmatrix}, \qquad \text{[S3]}$$

with different coefficients, μ_c, to take into account the fact that different species will partition to different extents between the oil and aqueous phases. The first step in LSA is finding the steady states, c_s, by solving analytically, $F_c = 0$. Next, the chemical rate equations (Eq. S2) are linearized about the steady state and the dynamics of a small perturbation $c_r = c_s + \delta c_r$ is explored in the linearized equations:

$$\partial_t \delta c_r = A\delta c_r + M_c(\delta c_{r-1} + \delta c_{r+1} - 2\delta c_r), \qquad \text{[S4]}$$

with $A = \partial f/\partial c$ the Jacobian matrix of equations (Eq. S2) with coefficients

$$a_{ij} = \left. \frac{\partial f_i}{\partial c_j} \right|_{c_s}. \qquad \text{[S5]}$$

To solve the linearized equations (Eq. S4), they are Fourier transformed by setting the following:

$$\delta c_r = \delta c_q e^{\sigma_q t} e^{iqr}, \qquad \text{[S6]}$$

with $q = 2\pi s/N$, where $s \in [0, s_{max}]$ is an integer with $s_{max} = N/2$ for N even and $s_{max} = (N-1)/2$ for N odd. This leads to the following eigenvalue equation:

$$0 = A - \sigma_q I - 4\sin^2\frac{q}{2}M_c, \qquad \text{[S7]}$$

from which the eigenvalue σ_q is found as a function of q. If all eigenvalues have negative real parts, there is a stable steady state. If one or more eigenvalue has a positive real part, then the steady state is unstable. The largest positive value of σ_q represents the fastest growing mode, and its q is associated with the corresponding Turing case. If σ_q is positive real, the Turing instability is nonoscillatory, corresponding to a "stationary Turing instability"; if σ_q is complex with a positive real part, then there is an "oscillatory Turing instability." The eigenvalue σ_q was found numerically using the parameters shown in Table S2 and a fixed ratio of $\mu_x = \mu_u/50$ and $\mu_y = \mu_z = 0$. Using Mathematica, we calculated the state diagram as a function of the bromine coupling strength, μ_u, and malonic acid (MA) concentration m, shown in Fig. 2 of the main text. There are no adjustable parameters in calculating the state diagram.

In more detail, when solving $F_c = 0$, we found six analytical steady states, which were then converted to numerical steady states and filtered to remove trivial and unphysical solutions. The remaining steady states (usually two, never more, occasionally only

one) were then categorized as reduced if $z_{ss} \approx c_{min}$ or oxidized if $z_{ss} \approx c_0$. The analytical Jacobian matrix was then converted to numerical Jacobian matrices using the parameters and steady-state solutions. The numerical Jacobian matrices and diagonal diffusion matrices were used to solve for the eigenvalues of each specified value of μ_u and m. Given two steady-state solutions for each parameter set and a four-variable system, each parameter set yields eight eigenvalues, and each eigenvalue is a function of the wavenumber q. The maximum value for the real component of each eigenvalue was calculated, and that with the largest real maximum was identified as the dominant mode. If all eight maximal real values were negative, then that case was identified as a stable steady state with no associated Turing pattern.

In Fig. 2A, along the left axis corresponding to low MA concentration (MA < 1 mM) and independent of coupling strength, there is one stable steady state corresponding to the oxidized state. Everywhere else, there are two steady states: one stable and oxidized, and the other unstable and reduced. Along the bottom axis, corresponding to zero coupling strength $\mu = 0$, LSA predicts that the unstable reduced steady state undergoes a nonoscillatory Turing instability [case (a)] for 1 mM < MA < 370 mM and an oscillatory Turing instability [case (b)] for MA > 370 mM. Away from the axes, the reduced steady state is unstable to one of the Turing instabilities corresponding to cases ($b–f$).

Once the dominant eigenmode was identified, that parameter set could then be further categorized. First, the wavenumber q_T at which the real maximum occurs is identified as the dominant wavenumber, and thus the associated Turing wavelength is $\lambda_T = 2\pi/q_T$. Second, the magnitude of the imaginary component of the dominant eigenvalue at the dominant wavenumber q_T is identified as the frequency ω_T. See Fig. S4 for examples. The six Turing states are defined by their dominant wavenumber q_T and associated frequency ω_T. However, given the numerical rounding and desire to compare with experiment, a small amount of leeway was allowed for defining states in the LSA. The mode was identified as stationary if $\omega_T < 10^{-7}$ rather than strictly equal to zero, the wavelength was identified as minimal if $\lambda_T < 2.02$ (measured in units of cell number) rather than strictly equal to 2, and the wavelength was identified as maximal if $\lambda_T > 39.6$.

Nonlinear Simulations. The simulations were conducted using the VE model, Eqs. S1 and S2, with the same parameters as used in the LSA (Table S2). The nonlinear simulations (NLSs) consisted of 40 identical BZ drops diffusively coupled through chemical species u (inhibitor) and x (excitator) with periodic boundary conditions. Different initial conditions were used for each drop and each trial. The initial conditions for the 40 drops were generated from a normal distribution (with coefficient of variation of 20% in each chemical species) around the steady state of the system. When the system oscillates, the reduced state of the oscillation has concentrations close to the steady state. For most of the state diagram, the steady state was unstable; only for extremely low values of MA was the steady state stable.

Numerical investigation of the NLS model revealed that MA concentration (m) and coupling strength (μ) are the two parameters that most greatly affect the state diagram of the system (Fig. 2 of the main text). To generate the NLS state diagram, we systematically varied the parameters μ and m and integrated equations (Eq. S1) long enough for the system to settle on a stable attractor. From the space–time plot, we could identify whether or not the attractor was a Turing state and to which case the attractor belonged. Similarly to the LSA, there are no adjustable parameters in calculating the nonlinear state diagram.

SI Discussion

Additional discussion of the concepts from the main text are included in this section.

Comparison with Data. When directly comparing the data from the synchronization rates of two drops and the state diagram measurements with the theoretical predictions, we found that an additional fitting parameter needed to be added for quantitative agreement between theory and experiment. As noted in the legend to Fig. S1, the coupling strength, μ, must be multiplied by a fitting factor of $f = 0.0152$ for the calculated and measured synchronization rates to match. The LSA and NLS are calculated in an abstract space where we vary the coupling strength μ_c over a range of values, whereas for experiments this is a function of many physical parameters (Eq. 2, main text) as derived earlier in this supplement. Similarly to the case of synchronization rates, in order for the state diagram data to match theory (Fig. 2), the coupling strength μ_c must be multiplied by a fitting factor of $f = 0.14$. Possible physical explanations for this fitting factor are mentioned in the main text. Furthermore, when plotting the data in Fig. 2 of the main text, the drop spacing is augmented such that $b = b + 10$ nm to account for the fact that drops do not coalesce, as they are always separated by a surfactant layer. Finally, when plotting 2D data in Fig. 2 of the main text, the coupling term μ is multiplied by 3 as a result of the normal mode analysis for closely packed spheres in 2D.

Observed States. We observe spatial-temporal patterns in drops arranged in linear rows, which are classified by their dimensionless wavevector, q, and oscillation frequency, ω, using the same nomenclature as Turing. The wavevector, q, has units of phase. Turing classified patterns by arranging the possible values of q into three categories: $q = 0$, $0 < q < \pi$, and $q = \pi$. Furthermore, Turing divided the frequency, ω, into two categories, $\omega = 0$ and $\omega > 0$. This scheme gives six cases in total, and we observe patterns with the symmetry of each of these cases, shown in Fig. 1. However, more than one distinct physical-chemical mechanism can lead to the same pattern; therefore, observation of a pattern with the same spatial-temporal structure as a Turing instability does not prove that the pattern arises from the Turing mechanism. To identify a pattern as a Turing instability, we additionally require that the observed pattern be located in the state diagram of Fig. 2*B* as predicted by the full Turing model. Our philosophy is that, if two predictions of the model agree with experiment, then the chances of the model being wrong are small. The ideal experiment would be to prepare the system in conditions corresponding to the unstable steady state and measure the chemical concentrations as a function of time. However, we do not have the ability to do this ideal experiment; the best we can do is observe the space–time pattern (Fig. 1) of the catalyst and the chemical state diagram (Fig. 2). Additionally, using a light-sensitive catalyst, for some set of parameters, we are able to control initial and boundary conditions, which permits careful experimental study of the coupling of two drops (Fig. S1).

The LSA and NLS calculations predict that, at very low MA concentrations, there is one steady state, corresponding to the oxidized state, and the steady state is stable. For a 1D array of drops, if all of the drops are stationary and in the same state (oxidized), then the wavevector ($q = 0$) and frequency ($\omega = 0$) correspond to the symmetry of Turing case (a). However, by definition, the state at low MA is not Turing state (a), because all Turing states must arise as an instability from an unstable steady state. Thus, for our system, only five of the six Turing states are predicted to exist. In experiment, we do observe a stationary, uniform state at low MA, exactly where theory predicts a stable steady-state solution. As experiment and theory agree, we assign this low MA to be the steady-state solution and not Turing state (a). However, for catalyst concentrations of 42 mM, which is 10 times the amount used in our experiments, the LSA predicts that, instead of the single, stable steady oxidized state found for MA < 1 mM, there are two steady states: one, the oxidized stable steady state, and a second unstable steady reduced state

with an instability to a nonoscillatory Turing instability corresponding to Turing case (a). Experimentally, when we prepared samples with catalyst concentrations exceeding 24 mM, in 20 mM MA, the samples did not oscillate, even though the VE model predicted they would oscillate. This discrepancy between theory and experiment is unresolved.

Of the remaining five Turing cases (b, c, d, e, f), four of the experimental Turing cases are observed to occur in the regions of the state diagram predicted by the NLS. Turing case (b) is an exception. At the experimental conditions for state (b) shown in Fig. 1 of the main text (2.4 M MA), the nonlinear simulations generate an initial transient state that corresponds to state (b), but that evolves with time into a stable attractor corresponding to Turing case (e). Notably, this evolution from an initial in-phase transient to Turing case (e) is also seen experimentally, but for much lower MA (20 mM) concentration, as shown in Fig. S3.

In summary, patterns with the same appearance as the six Turing cases (a–f) are observed as illustrated in Fig. 1. Five of the six patterns, Fig. 1 *A* and *C*–*F*, appear where predicted by theory. Four of the six patterns are identified with Turing cases (c, d, e, f). Turing case (a) does not occur for the parameters accessible to our experimental system. However, at low MA, we do observe a pattern with the same symmetry as Turing state (a), which the Turing model predicts to be a stable steady state. Only the pattern with the symmetry of Turing case (b), shown in Fig. 1*B*, is observed in a region of parameter space not predicted by theory.

The LSA unambiguously reveals the stability of the steady state and the eigenvalue of the instability for each chemical condition. The nonlinear simulations and experiments are more difficult to analyze, as the initial, linear response of the experimental system produces too small a signal to be detected with our instrumentation. In experiment, we observe dynamics when the chemical amplitudes are large and therefore non-linear. Identification of the Turing state is done using space–time data, which creates several difficulties. First, the drops are a closed chemical system. With time, the MA is consumed, but the coupling strength remains the same. In terms of the state diagram shown in Fig. 2, this means that conditions initiate from a starting point on the right of the figure, and with time evolve horizontally to the left. Second, the Turing states are dynamical attractors, but, in general, initial conditions of the NLS and experiments are different from the attractor, so that there is an initial transient period before the system settles in on an attractor. Third, wavelength selection is broad. This means that more than one wavelength will be selected, which leads to creation of defects in the patterns, complicating identification of states.

Four of the Turing states are straightforward to recognize and categorize, as they have finite wavelengths; these correspond to Turing states (c) and (d) (stationary with wavelengths of $\lambda = 2$ drops or $2 < \lambda < \infty$) and Turing states (e) and (f) (oscillatory with wavelengths of 2 drops $< \lambda < \infty$ or $\lambda = 2$ drops). The remaining two states [(a) and (b)] are more difficult to identify due to ambiguities and possible secondary mechanisms. In simulations, oscillations with nearest neighbors in-phase with each other are seen both as a final state [Turing state (b)] and as a transient response evolving to a finite-phase oscillatory state with nearest neighbors not in-phase [Turing state (e)]. This makes it difficult to classify in experiments whether what is seen is an adiabatic transition from a quasistable in-phase attractor to the finite-phase attractor due to decaying MA concentration, or an in-phase transient transforming to the finite-phase attractor. Experiments from high MA concentrations (2.4 M, Fig. 1*B* in the main text) demonstrate long periods of in-phase oscillations, lending support for transitions due to MA decay rather than initial transients. In general, if a system stays in one state for 10 periods, we consider this to be a stable attractor and not transient behavior resulting from initial conditions. Similarly, in simulations and experiments the in-phase stationary state is seen,

but it is impossible to determine by the space–time data alone if this is due to the Turing mechanism or an underlying stability of the steady state. In Fig. S5, we observe a transition from the finite-phase stationary state to the in-phase stationary state. Because the theory predicts a stable steady state at low MA, we conclude that experiment is consistent with theory and that what we observe is a steady state and not Turing state (*a*). Thus, although we present data and simulations that demonstrate the phenomenology of Turing state (*a*), it is the one state that we cannot classify as due to the Turing mechanism.

We repeated the experiments many times to average over transients. We also made samples with slightly different droplet diameters and spacings at constant chemical concentrations, and conversely, samples with the same droplet dimensions, but with slightly different chemical concentrations. In this way, we traversed the state diagram in Fig. 2*B* along vertical and horizontal trajectories. We compared the initial behavior of samples with slightly different MA concentrations, say 40, 30, and 20 mM, with a single sample of 40 mM malonic as a function of time. The hypothesis is that the sample that initially started at 40 mM MA would over long times lower its concentration from 40 to 30 and 20 mM and thus over time generate the states exhibited by fresh samples that initially had different MA concentrations. Only after a series of such experiments produced consistent results did we ascribe a Turing state to a particular region of the parameter space in Fig. 2*B*.

Finite Rings. An important facet to note is that the behavior of finite rings with a small number of oscillators depends on both the chemical conditions and the number of drops in the ring, as seen in Fig. 1 of the main text and Fig. S4. In a ring with an infinite number of drops, LSA allows continuous values of q and associated wavelength ($\lambda = 2\pi/q$); thus, the dominant mode is simply the q at which the real component of the eigenvalue is maximal. However, for finite rings, the wavelength is limited by the requirement of periodicity such that $q = 2\pi s/N$ for $s = [0, s_{max}]$, where for even-numbered rings, $s_{max} = N/2$, and for odd rings, $s_{max} = (N-1)/2$, as the phase differences between nearest neighbors around the ring must add up to an integer multiple of 2π. This yields the result that, for chemical conditions where the real component of the eigenvalue is maximal at $q = \pi$, there will be a different state for rings where N is even or odd, as $q = \pi$ is not an available solution when N is odd. In Fig. S4, we can see the predicted behavior for rings with three, four, five, and six drops and the corresponding experiments. In these situations, the linear stability predictions of the Turing theory and experiments are in complete agreement.

0sπs and 00ππ States. Another two states observed in simulations and experiments are what we refer to as the "0sπs" state and "00ππ" cluster state (as seen in Fig. 2 of the main text). The 0sπs state is a 1D state with a wavelength of four drops, of which the first and third drops are antiphase, whereas the second and fourth drops are stationary. The name 0sπs is simply a sequential observational naming scheme of zero phase, stationary, π phase, stationary. Examples of this state are shown in Fig. S6. From a linear stability point of view, this state would correspond to an oscillatory state with a wavelength of four drops, the same as a traveling wave; therefore, this state satisfies the normal mode solutions from Turing with nodes of zero amplitude located on the second and fourth drops, Turing state (*e*). Similarly, the 00ππ state has a period of four drops. However, all drops oscillate; the first two drops are in-phase and the next two drops are antiphase. These two states were seen in simulations before any experiments were done at the conditions at which the simulations identified the states. Subsequently, experiments found the state as predicted.

MA Decay. A key difference between the VE model and experiments is MA decay. The VE model is based on an open BZ reaction system where the reactors are continuously fed new reactants and products are continuously removed; the feed chemicals can be treated as constant. The experimental emulsion system is a closed BZ reaction where the reactants are consumed, and thus the chemical parameters change with time. Consequently, the MA concentration will decay with time. This allows for a single experiment to probe the state transitions that occur when the MA concentration crosses the border between two predicted patterns as seen in Fig. S5. The transitions observed are in agreement with the simulations based on the VE model as seen in Fig. 2 of the main text and are thus seen as additional confirmation that the underlying mechanism is indeed that described by Turing. We note that the bromate also decays in time, but because it is larger than the MA concentration (and the state behavior is less sensitive to it), this effect can be neglected.

Stabilization of the s0π State. The s0π state is observed in 2D hexagonal closed-packed lattices of BZ drops in the part of the state diagram shown in Fig. 2 intermediate between the Turing state (*d*) of stationary drops and Turing state (*e*) of oscillatory drops. It consists of a mixed oscillatory and stationary state in which three drops, arranged in a triangle, exhibited the following behavior: one drop was stationary, *s*, in a reduced, near stable steady state, and the other two oscillated π radians out of phase.

Considerable effort was spent trying to find parameters in numerical simulations in ordered, hexagonal arrays of drops that demonstrated the s0π state without the addition of heterogeneity, using both point models in Matlab and full finite-element simulations in COMSOL. All of these efforts proved futile, even with the inclusion of the ∼5% chemical and physical heterogeneity measured in experiments. For example, when we simulated a ring of three identical drops, we observed three different states as a function of coupling strength. At low coupling strength, all three drops oscillated with a relative phase shift of $2\pi/3$. At higher coupling strength, all drops continued to oscillate, but two drops had a relative phase shift of 0 and the third drop had a phase shift of π. At still higher coupling strength, the three drops stopped oscillating simultaneously. Only with the inclusion of exaggerated heterogeneity of ∼20% in either chemistry or geometry is the s0π state realized in simulations. In simulations, we have not yet explored the effect of lattice disorder on the state behavior, and at this point our understanding of the state is incomplete. What follows is our current best understanding of the state from a purely mathematical perspective.

To understand the origin of the s0π state, we first consider the oscillating pair. Two identical oscillators that are diffusively coupled such that the diffusivity matrix, M_c, in Eq. **S1** is scalar (each component has exactly the same diffusion coefficient) will always have a stable synchronized solution. Thus, to disrupt the synchronous state, the diffusion coefficients must be different, and if that is the case, then it is often possible to obtain a stable antiphase state when the two oscillating drops are coupled. In the VE model used here for illustration, the interdrop flux of the *u* component (bromine, inhibitor communicator) is far greater than that of the *x* component (bromous acid, activator). The origin and stability of the antiphase state can best be understood with the theory of weakly coupled oscillators, which enables one to write explicit equations for the phase differences between two or more oscillators when the coupling between them is sufficiently small. For the VE model, weak diffusion solely of *x* leads to stable synchrony and unstable antiphase behavior, whereas coupling via solely *u* or *z* leads to stable antiphase coupling. This is why we need a component of diffusion in the *u* variable.

With these preliminaries, we now assume that there is a pairwise antiphase stable state that can be extended into the weak coupling regime (that is, it remains stable as the diffusion strength

goes to zero). If we vary the parameter h, which controls the hydrogen ion concentration, we find that for $h < h_B$, where $h_B \approx 0.054$ (Fig. S7B), the oscillation of one drop ceases and there is a stable reduced steady state (stable equilibrium). The drop is dead. As h increases, the oscillation returns through a Hopf bifurcation (stable oscillations in Fig. S7B), where it persists beyond $h = 0.3$. Now, suppose that there is heterogeneity in the coupled set of three droplets. Let $h_1 = h_2$ and $h_3 < h_1$. This means drop 3 is closer to the stable reduced state. Indeed, if $h_3 < h_B$, then for this isolated drop, it is stable and dead. With small enough coupling between the three drops, because of our assumption about the pairwise stability of antiphase, we obtain a stable $s0\pi$ state. However, this is "cheating" because the third drop is in a stable steady state. Thus, we start to increase h_3 past the value h_B, which destabilized the reduced state. Clearly, if the coupling is too small, the pair of oscillating drops cannot stabilize the steady state. However, if the diffusion increases enough, it may be possible, and indeed, it is.

Using the VE system, we can fix $h_3 = 0.11$ to be close to, but above h_B so that, without coupling, drop three will undergo oscillations. We fix $h_{1,2} = 0.16$, so drops 1 and 2 also oscillate. For small diffusion, the interactions between the pair of oscillating drops (drops 1 and 2) can be predicted through a weak-coupling analysis. Fig. S7C shows the interaction functions resulting from coupling via x (black, scaled down by a factor of 10) and via u (red). Intersections with zero that have positive slopes represent stable locked states. Thus, coupling only via u leads to a stable antiphase state, whereas coupling via x encourages synchrony. Because the effects of x are an order of magnitude larger than those of u, the permeability of x must be greatly reduced to ensure that the pairwise coupled drops oscillate in antiphase. So, for small coupling, we satisfy the requirements for a $s0\pi$ state to exist when the diffusion is small. However, this state is not stable for very small diffusion because drop three is positioned at an unstable reduced state. Thus, we begin to increase the diffusion and find that if the heterogeneity is enough (h_3 sufficiently different from $h_{1,2}$), then the $s0\pi$ state is stabilized. As the diffusion gets larger, this state remains stable until the diffusivity is large enough to destroy it. For the VE model, if the diffusion is large enough, the antiphase state loses stability and becomes a synchronous state. Thus, the triplet will go to a state where the homogeneous pair synchronizes and the third drop oscillates occasionally, an example of $n:1$ mode locking. Other complex dynamics can also occur.

The mechanism for the stabilization of the $s0\pi$ state is not trivial. One could imagine, for example, that the diffusion terms, $-d_x x$, $-d_u u$, could stabilize the rest state, but it is easily checked that the strength of diffusion is much too small to have any effect. To better understand the phenomenon, we use the simplest possible model that has a Hopf bifurcation and the ability to oscillate pairwise in antiphase as follows:

$$z_j' = z_j \left[\mu_j - |z_j|^2 + i\left(1 + q|z_j|^2\right)\right] \\ + d(1+i\nu)\left[z_{j+1} + z_{j-1} - 2z_j\right] \quad j = 1, 2, 3. \tag{S8}$$

Here, we identify $j = 0$ with $j = 3$ and $j = 4$ with $j = 1$. These equations arise from doing a perturbation analysis around any system of coupled differential equations that undergo a Hopf bifurcation. The parameter μ_j plays the role of h_j in the VE model; for $\mu_j > 0$, there is an oscillation and otherwise a stable rest state. The parameter d is the net diffusivity. The parameter q provides amplitude dependence on the frequency of the oscillation, whereas the parameter ν plays the role of the different diffusivities of the four species in the VE. It is easy to write

down an exact expression for the $s0\pi$ state and then use standard stability theory to show conditions under which it is stable.

We can think of two ways to obtain a stable $s0\pi$ state in a ring of three oscillators without heterogeneity, but only if we allow the removal of some of the experimental constraints. For example, if the Hopf bifurcation is subcritical and then turns around (so that there is a regime of bistability between rest and oscillation; also called a "hard excitation"), then we can find a set of parameters such that the homogeneous model:

$$z_j' = z_j \left[\mu + |z_j|^2 - |z_j|^4 + i\left(1 + q|z_j|^2\right)\right] \\ + d(1+i\nu)\left[z_{j+1} + z_{j-1} - 2z_j\right] \quad j = 1, 2, 3$$

has a stable $s0\pi$ state and such that when $d = 0$, all three droplets oscillate. The VE model does not have this bistable region, so the simple model above violates the conditions imposed by the experimental system. Golubitsky et al. (3) (chapter XVIII, section 4, p. 393) provide a homogeneous version of Eq. S8, which exhibits a $s0\pi$ state; however, in the absence of diffusion, each droplet has only one stable steady state, again contradicted by experiment. The mechanism for the Golubitsky $s0\pi$ state is through a Turing–Hopf bifurcation to the rotating wave and then complex bifurcation involving a torus instability that ends with the $s0\pi$.

Morphogenesis. The experiments for this section are illustrated in Fig. 4 of the main text and Movie S7. Consider the net reaction in the FKN (4) model of the BZ reaction:

$$3BrO_3^- + 5CH_2(COOH)_2 + 3H^+ \\ \rightarrow 3BrCH(COOH)_2 + 2HCOOH + 4CO_2 + 5H_2O. \tag{S9}$$
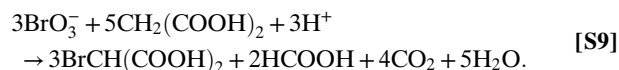
We assume that this is the major reaction that takes place in going from the reduced to the oxidized state. With the initial concentrations used, we have to take into account the counterions (every BrO_3^- comes with an Na^+, H^+ comes from H_2SO_4) and the sulfuric acid starts off as $H^+ + HSO_4^-$, but HSO_4^- dissociates to $H^+ + SO_4^{2-}$ when the reaction consumes H^+. The limiting reactant is the MA. If the reaction goes to completion in the oxidized state, all of the MA is consumed. We assume that essentially all of the CO_2 partitions out of the drops. The initial and final concentrations are shown in Table S3.

If we further assume that the drops in the reduced state consume no MA and the drops in the oxidized state go to completion, then this calculation shows that the maximum difference in molarity is 17% between a reduced and oxidized drop. This difference in molarity will drive a flux of water between the drops until the molarity of the drops is equal. In the experiment, roughly two-thirds of the drops are oxidized and one-third reduced. This leads to the prediction that the oxidized drops shrink by 6% in volume and the reduced drops swell by 12% in volume. The drops have a measured diameter of ~60 μm and they are confined in a rectangular capillary of 50-μm height. Assuming the drops are spheres leads to the prediction that the ratio of the radii of the swollen (reduced) to shrunken (oxidized) drops is 1.06, whereas assuming the drops are highly confined in height to be approximated as disks, the ratio of radii becomes 1.09. The measured ratio is 1.1, consistent with the crude estimates given above. Additionally, we can think of no other plausible mechanism to account for the change in size of the drops besides osmotic pressure. The combination of the reasonable physical mechanism and agreement between quantitative prediction and measurement leads us to conclude that osmosis drives the shape change, as speculated by Turing.

1. Israelachvili JN (2011) *Intermolecular and Surface Forces* (Academic, Oxford), 3rd Ed.
2. Cross M, Greenside H (2009) *Pattern Formation and Dynamics in Nonequilibrium Systems* (Cambridge Univ Press, Cambridge, UK), 1st Ed.
3. Golubitsky M, Stewart IN, Schaeffer DG (1988) *Singularities and Groups in Bifurcation Theory* (Springer, New York), Vol 2.
4. Noyes RM, Field RJ, Köros E (1972) Oscillations in chemical systems. I. Detailed mechanism in a system showing temporal oscillations. *J Am Chem Soc* 94(4):1394–1395.
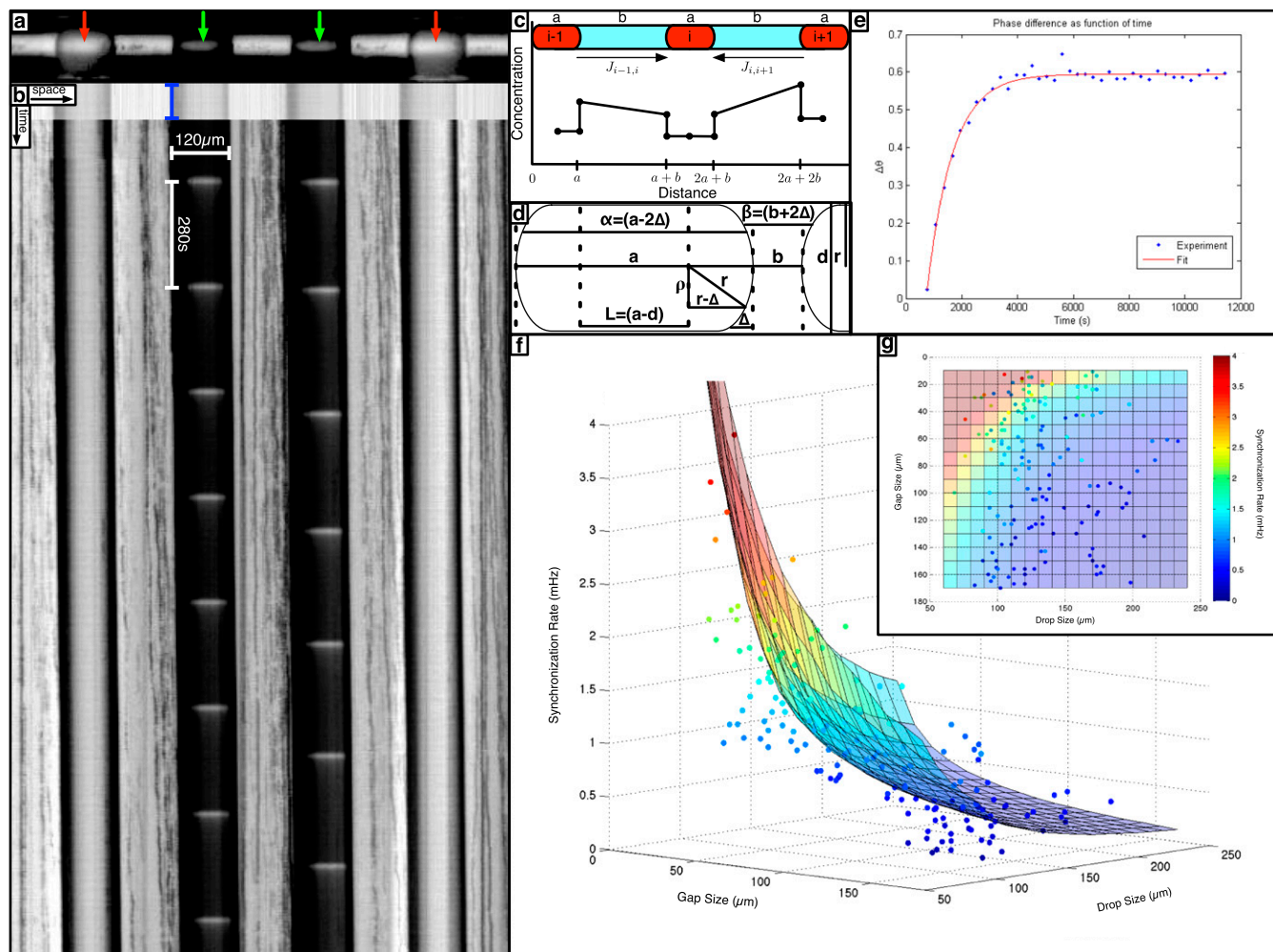
Fig. S1. Comparison between theory and experiment for the rate of synchronization between two isolated oscillating drops as a function of oil gap and drop size. (*A*) An image of four drops in a capillary where red arrows indicate drops inhibited with light and green arrows indicate drops allowed to oscillate. (*B*) A space–time plot demonstrating the initial bright pulse synchronizing the drops in phase (blue bar), the constant light holding the outer two drops in the oxidized state, and the phase evolution of the center two drops. Space–time plots were generated by plotting the intensity of a single line of pixels connecting the centers of adjacent drops as a function of time. See Movie S1. (*C*) A cartoon illustrating the assumptions in deriving Eq. **S2**, μ_c. (*D*) A schematic illustrating the geometry behind the Derjaguin approximation (1). The Latin characters (*a*, *b*, *d*, *L*, *r*) represent the experimental parameters including the measurements of end-to-end drop width *a*, end-to-end gap width *b*, capillary diameter *d*, and calculated parameters of the linear portion *L*, and radius of curvature *r* of the spherocylinder. The Greek characters (α, β, Δ, ρ) represent the internal variables of drop width β, gap width β, gap augment Δ, and radial position ρ. (*E*) A plot of the phase difference between the center drops from *Inset* (*A*) fit with an exponential curve from which the measured synchronization rate is extracted. (*F*) A 3D plot of the experimental rates plotted against the theoretical synchronization rates calculated for the coupling function μ_c of Eq. **S2** with the drop size and oil gap as independent variables. (*G*) A plan view of the same data as *Inset* (*F*). Obtaining agreement between the experimentally measured rates (*E*) and theoretically calculated rates (*F* and *G*) requires a scaling factor, $f = 0.0152$ in μ_c. Experimental conditions: 300 mM bromate, 3 mM ferroin, 1.2 mM Rubpy, 80 mM acid, 400 mM MA, 10 mM NaBr, 100-μm round capillary, ~100-μm drops, and ~105-μm gaps.
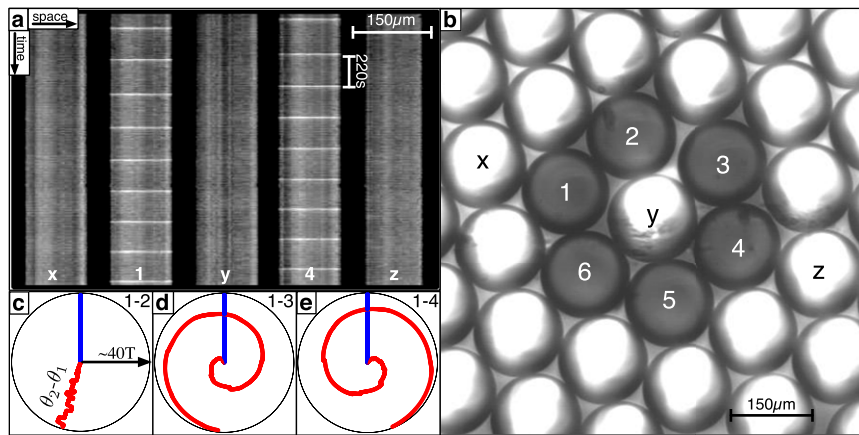
Fig. S2. Optical isolation is achieved by using the fact that illuminated drops have constant chemical conditions corresponding to the reduced state. (*A*) A space–time plot of the drops *x*-1-*y*-4-*z* shown in *B*. For this space–time plot, all but drops 1 and 4 were illuminated. Drops 1 and 4 oscillate; the rest were held constant in the reduced state. (*B*) An image illustrating the selective illumination of droplets to create a ring of six drops. (*C–E*) Radial phase-time plots of optically isolated drops (time is the radial dimension, zero in the center, and phase is relative to drop 1). In each plot, only two drops are allowed to oscillate; all others are optically inhibited. These experiments last ~40 drop periods. (*C*) Drops 1–2 are phase locked with a phase difference of ~170°. (*D* and *E*) Drops 1–3 and drops 1–4 are asynchronous and drift ~2π out of phase after ~40 periods. All drops contain 300 mM bromate, 3 mM ferroin, 1.2 mM Rubpy, 80 mM acid, 400 mM MA, and 10 mM NaBr. Drop size is ~150 μm.
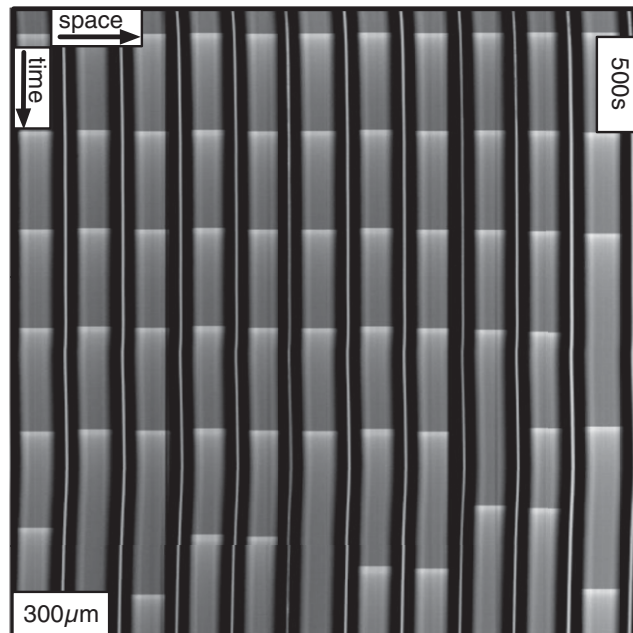
Fig. S3. Space–time plot illustrating transient behavior. Drops, in conditions corresponding to Turing case (*e*) were initiated all in phase by application of a long pulse of light. After two oscillations the system adjusts to Turing instability (*e*), (*q,ω*). Chemical conditions: 20 mM MA, 80 mM H_2SO_4, 300 mM $NaBrO_3$, 3 mM ferroin, no NaBr, 0.4 mM Rubpy, drop size of ~140 μm, and oil gap of ~10 μm.
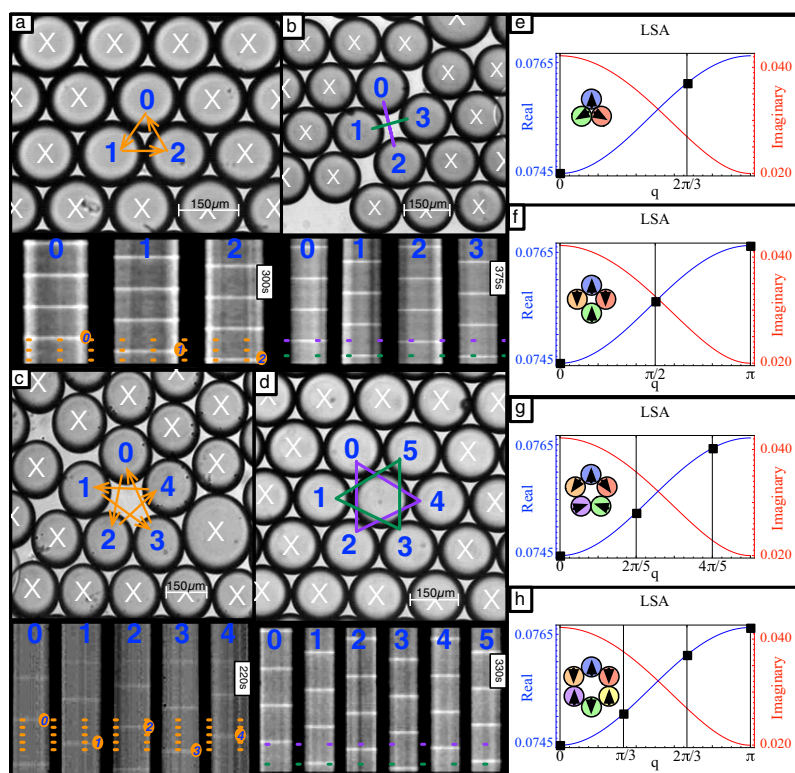
Fig. S4. Comparison between theory and experiment for rings of 3, 4, 5, and 6 drops. (*A–D*) Photoisolated rings of BZ drops with space–time plots to indicate order of oscillation. (*E–H*) LSA predictions for finite rings with allowable states indicated with squares. Allowable wavenumbers correspond to $q = 2\pi s/N$, where the integer s ranges from 0 to s_{max}, where for even-numbered rings $s_{max} = N/2$ and for odd rings $s_{max} = (N-1)/2$. The wavevector with the largest real value grows the fastest. All of the wavevectors are imaginary and therefore oscillate. Conditions as shown in Table S1 for Turing instability *f*. See *SI Methods* for details on the LSA plots.
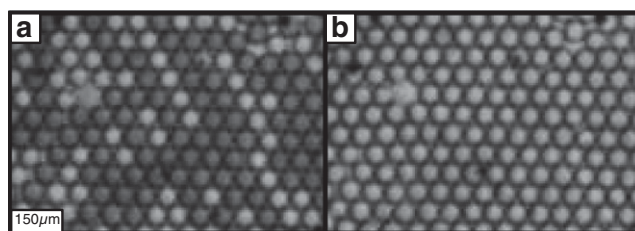
Fig. S5. The MA concentration of a closed reaction decreases with time such that the system evolves along horizontal trajectories proceeding from *Right* to *Left* in Fig. 2 and can undergo a transition from one Turing instability to another. The initial chemical conditions are 80 mM H_2SO_4, 300 mM $NaBrO_3$, 40 mM MA, 3 mM ferroin, no Rubpy, and no NaBr. Drop size is ~50 μm, and oil gap is ~0 μm (touching) corresponding to $\mu = 1$ in a wide flat 2D capillary. (*A*) Image of the system at an early time, which corresponds to Turing case (*d*), or (finite wavevector, stationary) denoted as (q,0). With MA ~40 mM and $\mu = 1$, the numerical simulations of Fig. 2 in the main text also predicts Turing case (*d*). (*B*) Image of the system 2 hours after *A*, which corresponds to a uniform state [or Turing case (*a*)], or (zero wavevector, stationary) denoted as (0,0). The numerical simulations of Fig. 2 in the main text predict a *stable* stationary (0,0) state at $\mu = 1$ for MA < 10 mM. Movie S4 of this data shows that the oxidized fraction increases gradually from that in *A* to that in *B*.
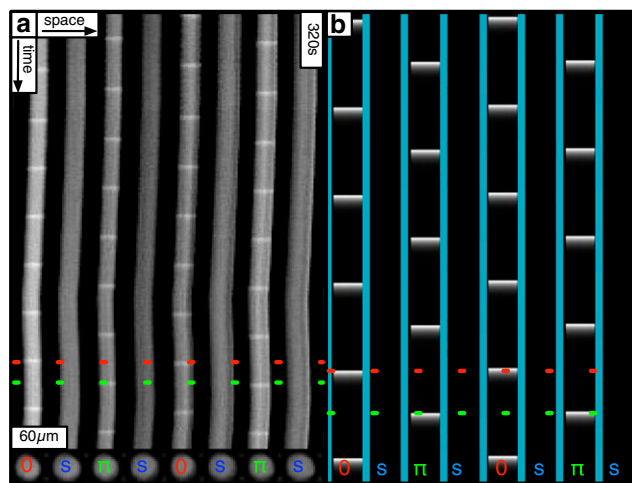
Fig. S6. Example of the 0sπs state in experiment and simulation. The red and green dashed lines are meant to guide the eye for the phase differences between oscillatory drops. (*A*) Experimental data demonstrating the 0sπs state. Experimental conditions: 400 mM MA, 80 mM sulfuric acid, 300 mM bromate, 10 mM bromide, 3 mM ferroin, 1.2 mM Rubpy, ~50-μm drop size, and ~3-μm spacing. (*B*) Numerical simulations demonstrating the 0sπs state. Simulation conditions: $m = 400$ mM MA, $h = 160$ mM H^+, $A = 300$ mM bromate, $c_0 = 4.2$ mM catalyst, $a = 50$-μm drops, $b = 50$-μm gap, $P_u = 2.5$, and $P_x = 0.05$.
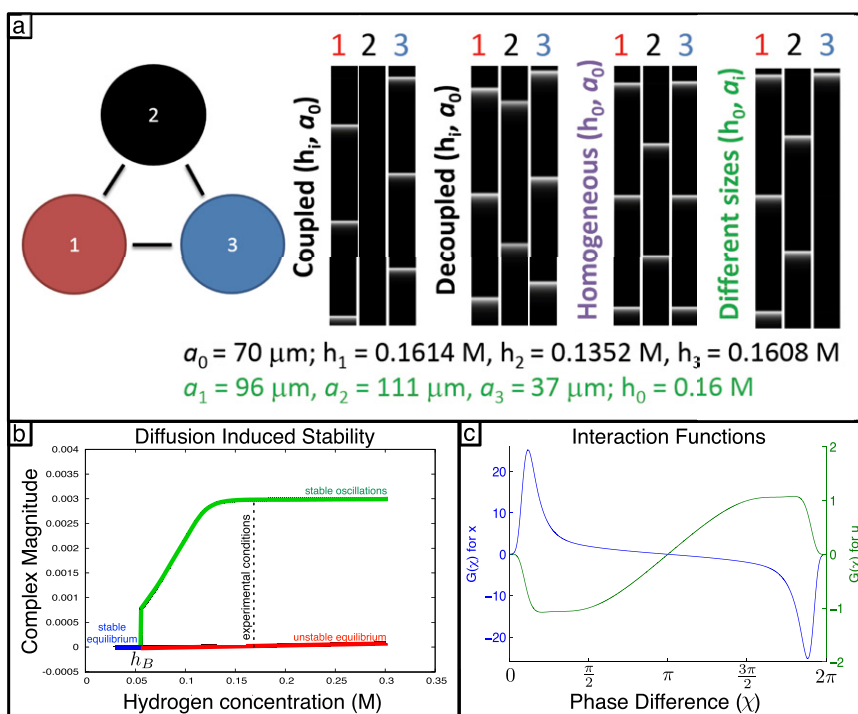
Fig. S7. In theory and simulation, the $s0\pi$ state is only seen in the presence of small chemical or physical heterogeneities. (*A*) Point oscillator VE model simulation for three BZ drops using periodic boundary conditions and random initial conditions close to the steady state. Parameters: $P_x = 0.05$, $P_u = 2.5$, $a = 70$ μm, $b = 0$ μm, $h_i = [H^+]_i$ for $i = 1,2,3$, $m = 640$ mM, $A = 300$ mM, $c_0 = 3$ mM. The simulated space–time plots indicate that, when coupled, the system with small chemical heterogeneity forms the $s0\pi$ state, when decoupled ($P_x = P_u = 0$) all three drops are oscillatory, and without chemical heterogeneity forms an anti-phase pattern. The $s0\pi$ state was also observed in systems with physical heterogeneity. (*B*) A bifurcation diagram demonstrating that at typical experimental conditions there is an unstable equilibrium state as well as a stable oscillatory state. (*C*) The interaction function for the u and x components of the VE mechanism.

Table S1. Experimental conditions for each observed state

State	MA	Drop, μm	Oil, μm	NaBr, mM	Rubpy, mM	Capillary
Turing *a*	10 mM	130	20	—	0.4	100 μm round
Turing *b*	2.4 M	230	100	10	0.4	100 μm round
Turing *c*	20 mM	98	0/47	—	0.4	100 μm round
Turing *d*	40 mM	95	0	—	0.4	100 μm round
Turing *e*	640 mM	117	3	10	0.4	100 μm round
Turing *f*	380 mM	106	25	10	0.4	100 μm round
Rings	640 mM	150	0	10	1.2	100 μm flat
s0π	640 mM	70	0	10	0.4	100 μm flat
Morpho	200 mM	66	0	—	0.4	50 μm flat

In all experiments, 80 mM sulfuric acid, 300 mM sodium bromate, and 3 mM ferroin were used. The addition of sodium bromide (up to 10 mM) has been seen to only change the initial conditions. The concentration of Rubpy (up to 2 mM) has been seen to only change the optical isolation capabilities.

Table S2. Simulation parameters and their experimental counterparts

Parameter	Counterpart	Value	Type
A	Sodium bromate	0.3	Constant
c_0	Total catalyst	0.003/0.0042	Constant
h	Hydrogen ions	0.16	Constant
m	MA	Varies	Constant
μ	Coupling strength	Varies	Constant
x	Activator $HBrO_2$	Variable	Intermediary
y	Inhibitor Br^-	Variable	Intermediary
z	Oxidized catalyst	Variable	Intermediary
u	Communicator Br_2	Variable	Intermediary

In the VE model, the inclusion of sodium bromide, only changes the initial value of y and Rubpy is not differentiated from ferroin as z is the sum of both catalysts. The physical parameters a, b, d, D, and P are included in the diffusion term μ as described in *SI Methods*. Other rate constants used are as follows: $k_1 = 2 \times 10^6$, $k_2 = 2h^2 A$, $k_3 = 3000$, $k_4 = 42hA$, $k_7 = 29m$, $k_{10} = 0.05m$, $k_r = 2 \times 10^8$, $k_{red} = 5 \times 10^6$, and $c_{min} = \sqrt{2k_r c_0 (k_9 + k_{10})/k_{red}^2}$. The value of k_9 depends on m such that $k_9 = 0.12m$ for $m > 0.1$ and $k_9 = 0.07m$ for $m \leq 0.1$.

**Table S3. Chemical concentrations for morphogenesis experiments**

Species	Initial concentration, mM	Final concentration, mM
Na^+	300	300
BrO_3^-	300	180
MA	200	0
H^+	80	40
HSO_4^-	80	0
SO_4^{2-}	0	80
BrMA	0	120
HCOOH	0	80
Total	960	800

The initial and final concentrations of the chemical species are indicated along with the net molarity within the drops.
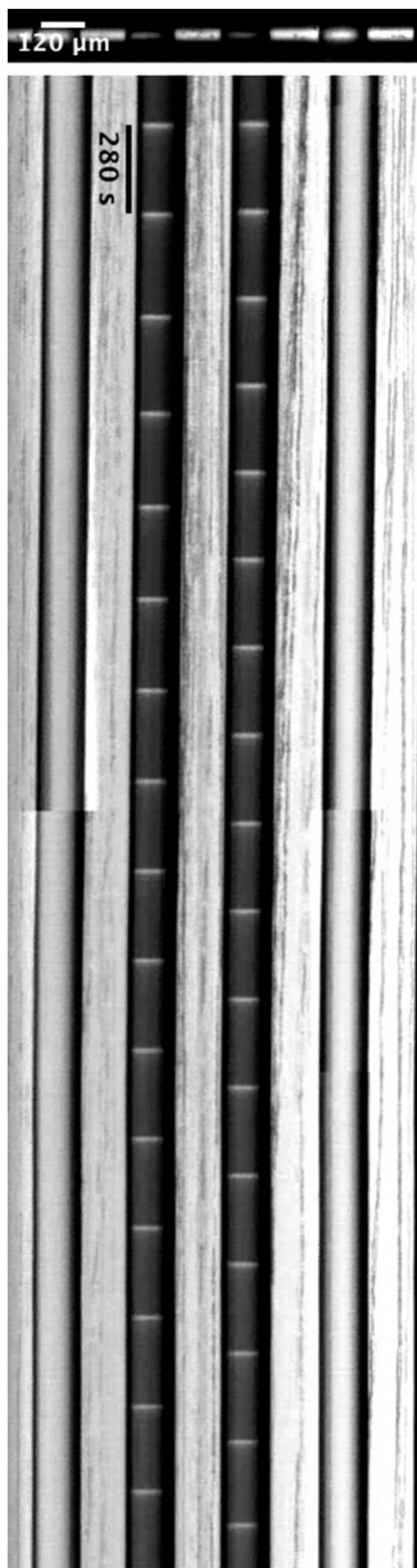
Movie S1. Data from extended data Fig. 1. The source data from Fig. S1 combined with an animated space–time plot of the same data. Four drops in a capillary with constant light holding the outer two drops in the oxidized state to measure the phase evolution of the center two drops, which are initially synchronized. Experimental conditions: 300 mM bromate, 3 mM ferroin, 1.2 mM Rubpy, 80 mM acid, 400 mM MA, 10 mM NaBr, 100-m round capillary, 100-m drops, and 105-m gaps.
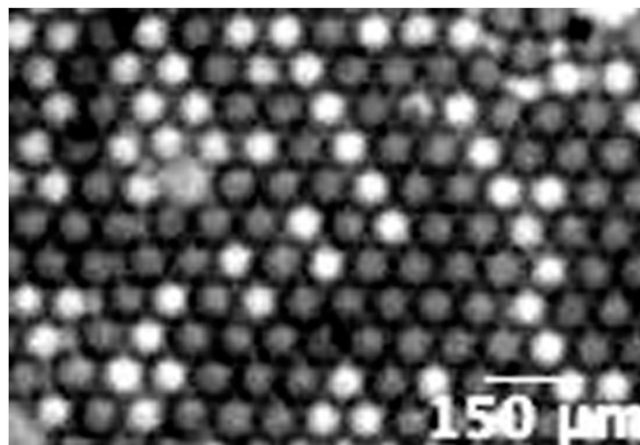
Movie S1
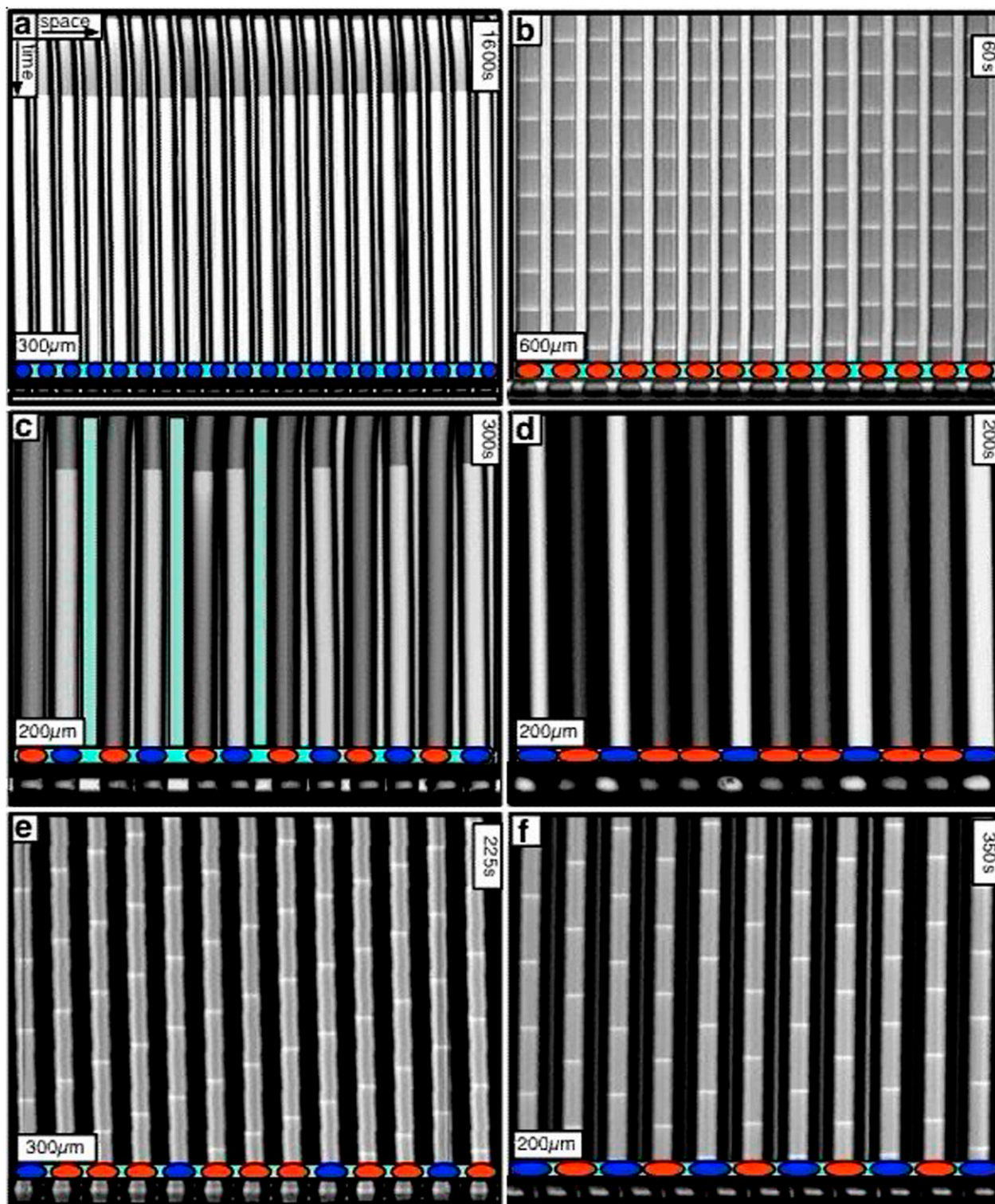
Movie S2. Data from Fig. 1 *A–F*. Fig. 1 *A–F* displayed with the movie accelerated 100×. Chemical states of linear arrays of BZ drops. (*A–F*) Cylindrical capillaries of 100-m inner diameter filled with a linear array of closely spaced droplets. (*Upper*) Space-time plot demonstrating Turing state. (*Lower*) Cartoon above corresponding movie of droplets. Cartoon colors: blue, BZ drops in oxidized state; red, reduced state; cyan, oil. Chemical conditions: 300 mM bromate, 3 mM ferroin, 0.4 mM Rubpy, and 80 mM sulfuric acid. Malonic acid (MA), NaBr, drop size and spacing specified in each case. (*A*) Stationary stable oxidized state after initial transient; 10 mM MA, no NaBr, drop size of 130 m, and oil gap of 20 m. (*B*) Turing case *b*, (long-wavelength, oscillatory), 2.4 M MA, 10 mM NaBr, drop size of 230 m, and oil gap of 100 m. (*C*) Turing case *c*, (short-wavelength, stationary), 20 mM MA, no NaBr, drop size of 98 m, and variable oil gap between 0 and 47 m. (*D*) Turing case *d*, (intermediate-wavelength, stationary), 40 mM MA, no NaBr, drop size of 95 m, and oil gap of 0 m (touching drops). (*E*) Turing case *e*, (intermediate-wavelength, oscillatory), 640 mM MA, 10 mM NaBr, drop size of 117 m, and oil gap of 3 m. (*F*) Turing case *f*, (short-wavelength, oscillatory), 380 mM MA, 10 mM NaBr, drop size of 106 m, and oil gap of 25 m.
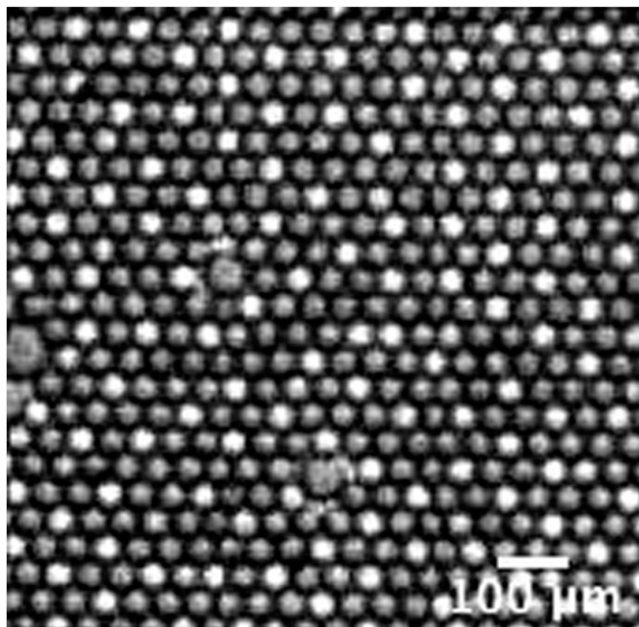
[Movie S2](#)
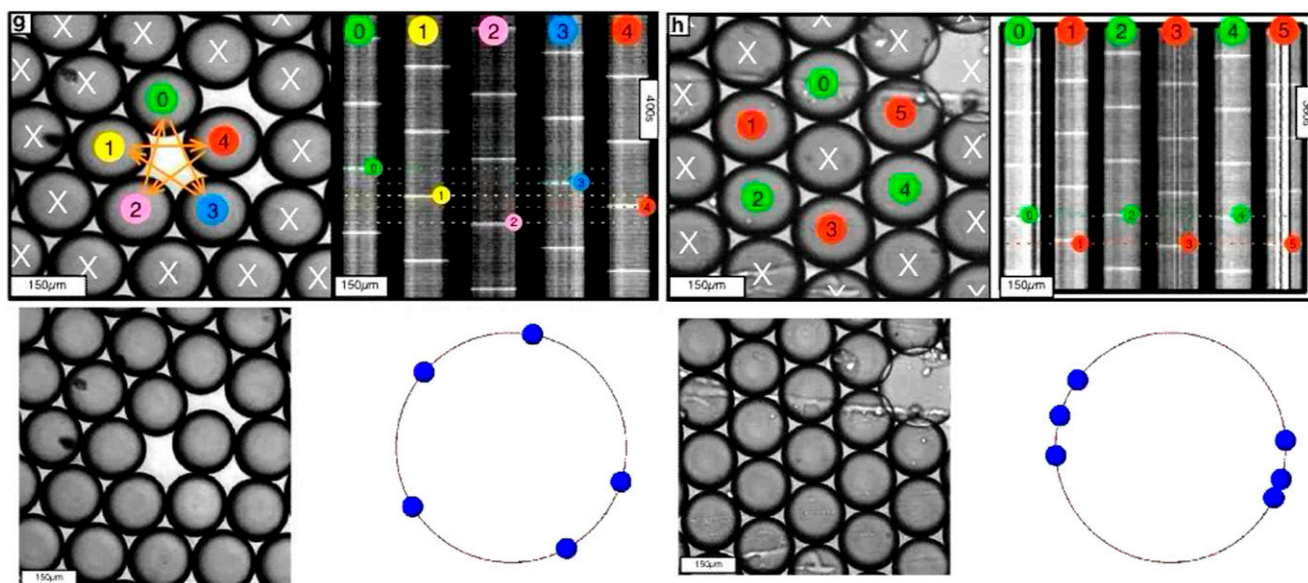
Movie S3. Data from Fig. 1 *G* and *H*. Fig. 1 *G* and *H* displayed with the source data at 300× and the phases of each oscillator plotted on the phase circle. (*G* and *H*) Odd and even circular arrays. Turing case *f*. Rectangular capillaries with cross-section 0.1 mm × 2 mm filled with a 2D array of close-packed droplets from which rings are created with optical isolation. (*Left*) Oscillatory drops are labeled; all other drops are illuminated with light (cross) and held nonoscillatory in the reduced state. (*Right*) Space–time plot. Chemical conditions: 300 mM bromate, 3 mM ferroin, 80 mM sulfuric acid, 10 mM NaBr, 0.4 mM Rubpy, 640 mM MA, and drop size is 150 m. (*G*) Five-membered ring. Drops oscillate in a pentagramal pattern. (*H*) Six-membered ring. Neighboring drops are radians out-of-phase.

[Movie S3](#)

Movie S4. Data from extended data Fig. 6. Extended data Fig. 6 source data accelerated 1,000× . The MA concentration of a closed reaction decreases with time such that the system can undergo a transition from one Turing state to another. The initial chemical conditions are 80 mM H_2SO_4, 300 mM $NaBrO_3$, 40 mM MA, 3 mM ferroin, no Rubpy, and no NaBr. Drop size is 50 m and no oil gap corresponding to $\mu = 1$ in a wide flat 2D capillary. At an early time, the system clearly corresponds to Turing state (*d*). With MA 40 mM and $\mu = 1$, the numerical simulations of Fig. 2 in the main text predicts the same Turing state (*d*). After about 2 h, the system is in a uniform state [or Turing state (a)]. The numerical simulations of Fig. 2 in the main text predicts this same state at $\mu = 1$ for MA < 10 mM.

[Movie S4](#)

**Movie S5.** Data complementing extended data Fig. 6. A $100\times$ accelerated movie showing initial transients transforming over time to a final Turing state (*d*). The system is initially entirely reduced until an oxidation wave oxidizes most of the drops. The oxidized drops then selectively reduce until only one-third of the drops remain oxidized in a well-ordered hexagonal pattern. Chemical conditions: 666 mM MA, 0 mM Rubpy, 0 mM NaBr, 80 mM H_2SO_4, 300 mM $NaBrO_3$, 3 mM ferroin, 0.05×1-mm capillary, initial drop size of 35 μm.

[Movie S5](#)
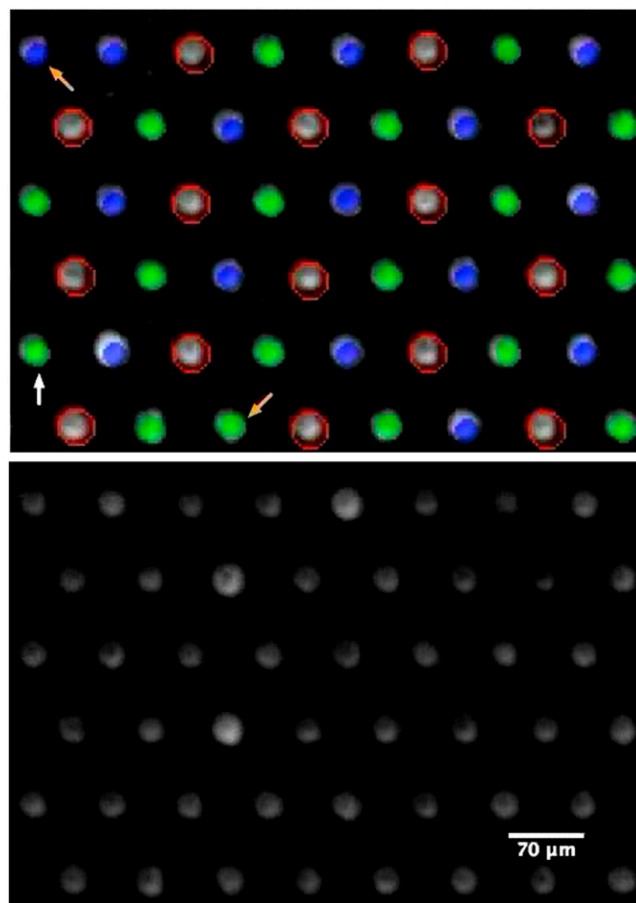
Movie S6. Data from Fig. 3. Movie of Fig. 3 source data accelerated 180× displayed with Fig. 3, *Inset D*. Observations of 2D arrays of s0π states. (*Upper*) A combined image in which the stationary drops are outlined in red and the oscillatory drops are color coded by their phase difference, $\phi = \theta - \theta_{ref}$, where $0 < \phi < \pi$ and θ_{ref} is the phase of the drop indicated with the white vertical arrow. Drops where $\phi < \pi/2$ are green and $\phi > \pi/2$ are blue. Notice that every third drop is stationary and every oscillatory drop is out of phase with its immediate neighbors, with two exceptions noted with orange arrows. (*Lower*) Movie of Fig. 3 source data accelerated 180× displayed with Fig. 3, *Inset D*. Chemical conditions: 300 mM bromate, 3 mM ferroin, 0.4 mM Rubpy, 80 mM acid, 640 mM MA, and 10 mM NaBr. Drop size is 70 m.

Movie S6
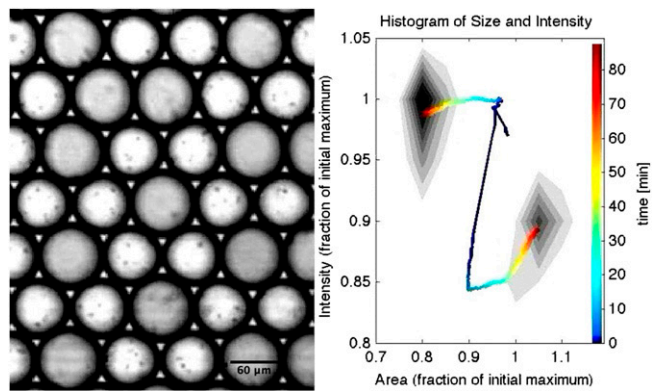
Movie S7. Data from Fig. 4. Movie of Fig. 4 and animated histogram displayed with a nonlinear timescale (time bar in movie). Drops demonstrating morphogenesis plotted as fraction of original drop area vs. fraction of original drop intensity. The color-coded line tracks the center of each peak as a function of time. Drops are initially homogenous in both intensity and size. Bright drops are oxidized, and dark drops are reduced. At intermediate times, the drops undergo a Turing case (*d*) instability; heterogeneous in intensity, or oxidation state, but homogenous in size. At later times, drops are heterogeneous in both oxidation state and size. The oxidized (bright) drops shrink and reduced (dark) drops swell. Chemical conditions: 200 mM MA, 0.4 mM Rubpy, 0 mM NaBr, 80 mM H_2SO_4, 300 mM $NaBrO_3$, 3 mM ferroin, 0.05 × 1-mm capillary, and initial drop size of ~66 μm.

[Movie S7](#)

Correction